Chapter 16

Fabrication of Semiconductor with Modified Microstructure for Efficient Photocatalytic Hydrogen Evolution Under Visible Light

Tao Yang, Xinmei Hou, Junhong Chen and Kuo-Chih Chou

Additional information is available at the end of the chapter

http://dx.doi.org/10.5772/63487

Abstract

Since sustainable energy and environment emerging as one of the top issues and challenges for humanity, the photocatalytic hydrogen evolution under visible light has attracted increasing attention. Basically the separation and transmission of photogenerated charge carriers are the two main steps of a photocatalytic reaction. They should be key aspects in the design of efficient photocatalysts for solar energy conversion.

3C-SiC is an important semiconductor with suitable band gap (2.3-3.3 eV) and excellent properties, especially the environmentally-friendly property. Titanium nitride (TiN) has a narrow energy band gap (0.80 eV) and good electrical conductivity. However, they as photocatalysts both do not draw wide attention due to the high recombination rate of photogenerated electron-hole pairs.

Herein B-doped 3C-SiC nanowires with finned microstructure were prepared through carbonthermal reduction combining the ion doping and morphology modification. It shows an outstanding activity toward H2 production as high as 108.4 $\mu mol \bullet h^{-1} \bullet g^{-1}$, which is 2.6 times of the value reported in the literature for SiC. TiOxNy/TiN heterojunction composite with tunable chamber structures were prepared through reduction and nitridation of organotitania. It demonstrates an outstanding photocatalytic activity as high as 34.9 $\mu mol \bullet h^{-1} \bullet g^{-1}$, which is about 1.5 times higher than the highest value reported in the literature for TiN.

Keywords: semiconductors, modified microstructure, plane-wave-density function theory, photocatalytic, hydrogen production

1. Background

In recent years, energy shortage and environmental pollution have become the focus of world attention. Overuse of fossil fuels is the main reason of these problems. Strong dependence on fossil fuels has also made our economy susceptible to price spikes and intensifying air pollution and global warming. Thus, developing a clean, renewable alternative to fossil fuels is a matter of utmost urgency.

The San Francisco earthquake with magnitude 7.8 in 1906 released an estimated 10^{17} joules of energy, the amount the Sun delivers to Earth in one second. So earth can get a staggering amount of energy, which was provided by the Sun. This energy can power the great oceanic and atmospheric currents, the cycle of evaporation and condensation of water, and the typhoons, hurricanes, and tornadoes. The 4.6×10^{20} joules, that humans use annually, is equal to the amount of energy that Earth get from the sun in one hour. The 1.2×10^{5} terawatts, which Earth gets from the Sun, is far above every other energy source [1]. And solar energy is one of the cleanest energy resources that does not compromise or add to the global warming [2]. It is often called "alternative energy" to fossil fuel energy sources such as oil and coal.

The impressive supply of solar energy is complemented by its versatility, as illustrated in **Figure 1**. Solar energy applications are divided into three main categories: yield of electricity by exciting electrons in a solar cell, yield of chemical fuel through natural photosynthesis in green plants or artificial photosynthesis in human-engineered systems, and production of heat using concentrated or unconcentrated sunlight for direct use or further conversion to electricity.

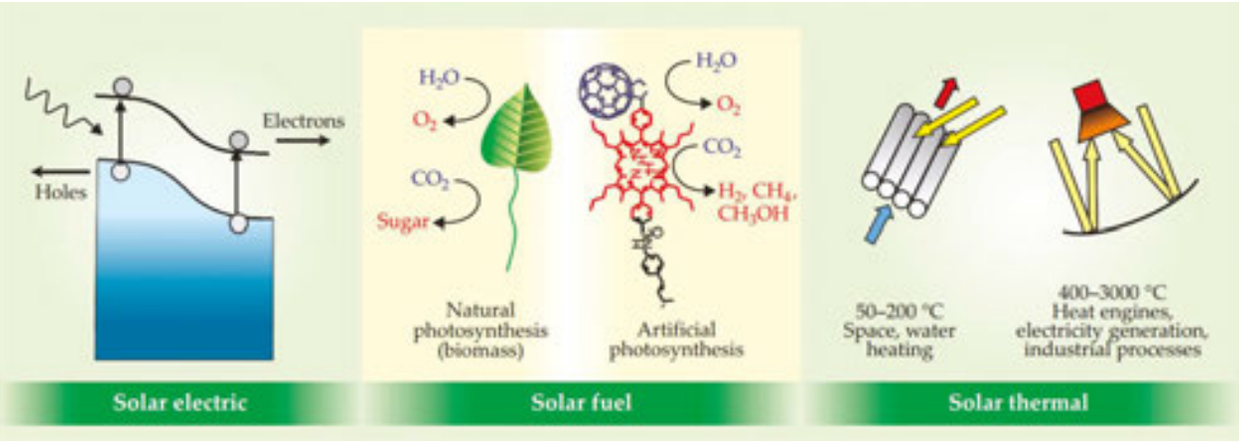

Figure 1. Solar photons convert naturally into three forms of energy – electricity, chemical fuel, and heat – that link seamlessly with existing energy chains [1].

Despite the abundance and versatility of solar energy, we use very little of it to directly power human activities. The reasons are these three main categories have their shortcoming, storage problems for solar electric, emission of greenhouse gases (mainly CO_2) for solar fuel and inefficient for solar thermal energies. So we must find ways to store the large quantities of electricity and heat when conversion on a large scale is achieved. Otherwise, solar energy is

http://dx.doi.org/10.5772/63487

an interrupted energy, which caused by natural cycles of cloudy-sunny and day-night variation, and energy demands are often out of phase with solar energy. Solar fuel production can store energy in chemical bonds. However, it is much more difficult to store electricity and heat. The task, that storing electricity or heat cost effectively for 24 h, is well beyond present technology. So we need a cleaner, more effective, and achieved storage method under present technology.

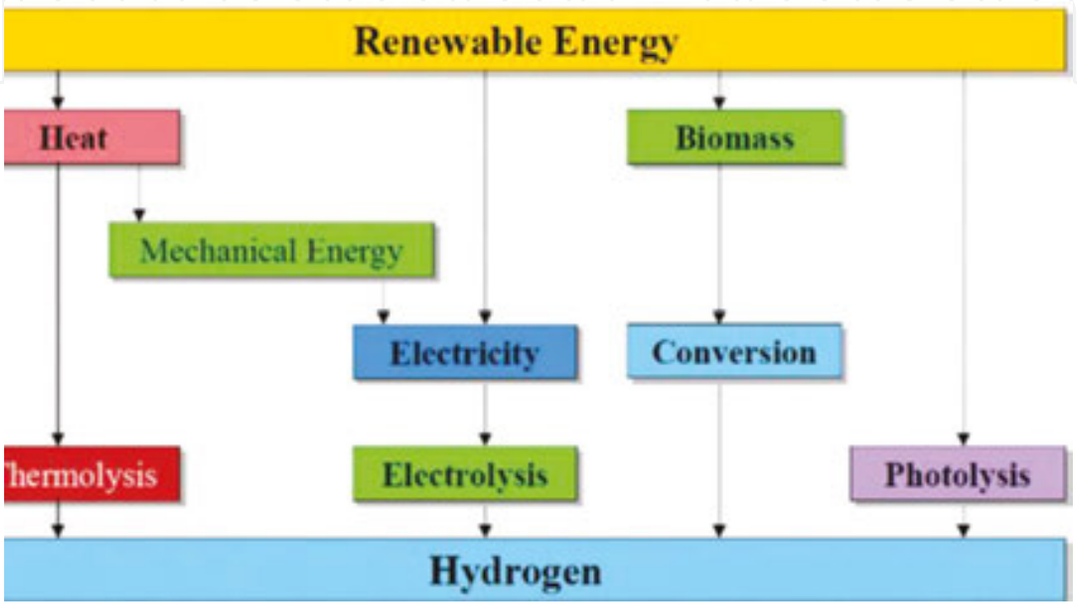

Figure 2. Sustainable pathways for hydrogen production from renewable energy, such as solar energy [10]. Copyright 2014 with permission from The American Association for the Advancement of Science.

Hydrogen is potentially an ideal energy carrier, as it is nonpolluting and gives up both its electrons upon oxidation to form only water. It may enable a secure and clean energy future, which uses hydrogen as the energy carrier connecting energy source to diverse end uses. Hydrogen is only an energy carrier for storing and transporting energy, which is different with oil and natural gas. Before we can use hydrogen, we have to produce it since hydrogen does not exist naturally. Every year, more than 500 billion cubic meters are produced [3, 4]. Most of this hydrogen is used for industrial purposes, such as refining petroleum and producing ammonia for fertilizers and other chemicals. In a hydrogen energy system, hydrogen containing compounds such as fossil fuels and water are potential sources of hydrogen [5, 6]. When hydrogen is derived from hydrocarbons, CO_2 capture and sequestration are requirements in a low greenhouse gas scenario [7, 8]. However, hydrogen produced from water does not present the challenge of unwanted emissions, but it does require an external resource [9]. If this energy can be obtained from a renewable energy source such as solar energy, hydrogen can then be considered a green energy alternative capable of powering everything. Otherwise, the storage problems of solar energy can be solved by hydrogen. Therefore, achievement of solar hydrogen production from water has been explored vigorously. Several ways for solar hydrogen production are applied (**Figure 2**) [10].

i. Electrolysis of water using a hydroelectric power generation, a solar cell, etc.

ii. Reforming of biomass.

iii. Photoelectrochemical or photocatalytic water splitting.

Since water electrolysis needs a large number of infrastructure constructions for clean power, the practical widespread application of this technique is constrained by its high cost. However, direct solar-to-hydrogen conversion based on photochemical and photoelectrochemical water splitting is a promising scheme for sustainable hydrogen production. Currently, direct solar-to-hydrogen conversion is in the conceptualization stage still, but ongoing technological progress will ultimately make this approach enter the stage of actual application in the future.

1.1. Fundamental mechanism of photocatalytic hydrogen generation [11]

Photocatalytic water splitting by solar irradiation is appealing and has been intensively studied in the last four decades [12, 13]. In Fujishima and Honda's pioneering work, they constructed an electrochemical cell for the decomposition of water into hydrogen and oxygen [14]. When the TiO_2 electrode was irradiated by light, oxygen evolution occurred at the TiO_2 electrode. Concomitant reduction led to hydrogen evolution at the platinum black electrode. After the photocatalyst absorbs photon from light source such as sun, the electrons in the valence band of the photocatalyst are excited to the conduction band, while the holes are left in the valence band (called the negative-electron (e^-) and positive-hole (h^+) pairs). The "band gap" is the energy difference between the valence band and the conduction band. And the light can be effectively absorbed by the photocatalyst, while the wavelength of it corresponds to the "band gap". After the excited electrons and holes are generated in photocatalyst, they separate and migrate to the surface. Here, they act as reducing agent and oxidizing agent to produce H_2 and O_2 in the photocatalytic water-splitting reaction. A schematic representation of the principle of the photocatalytic system for water is depicted in **Figure 3**.

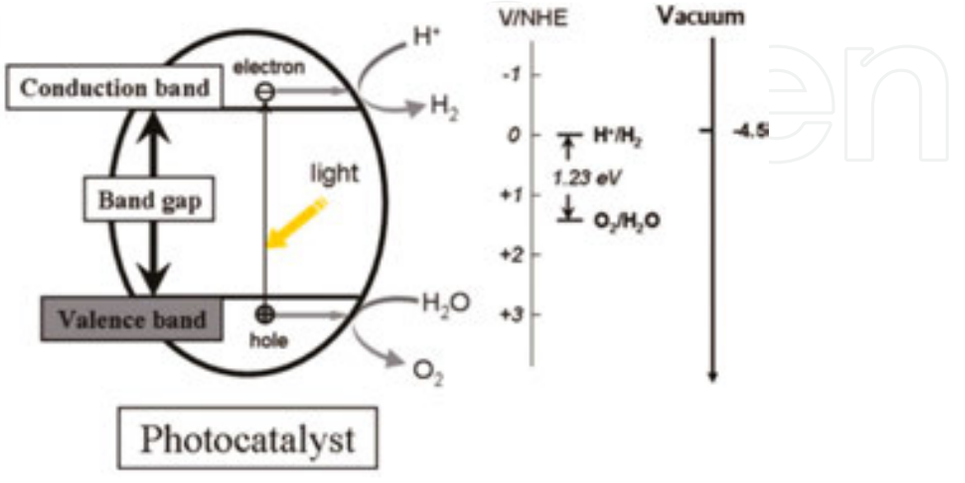

Figure 3. Fundamental principle of semiconductor-based photocatalytic water splitting for hydrogen generation [11].

http://dx.doi.org/10.5772/63487

Water splitting into H_2 and O_2 is an uphill reaction. It needs the standard Gibbs free energy change ΔG^0 of 237 kJ/mol or 1.23 eV, as shown in **equation 1**.

$$H_2O \rightarrow 1/2O_2 + H_2;\ \Delta G = 237000\ J/mol \quad (1)$$

Therefore, to achieve water splitting, the band gap energy of the photocatalyst should be>1.23 eV (<1000 nm) and it should be <3.0 eV (>400 nm) to use visible light.

The proper band gap and the potentials of the conduction and valence bands are important to facilitate both the reduction and oxidation of H_2O. The top level of the valence band has to be more positive than the oxidation potential of O_2/H_2O (1.23 V), and the bottom level of the conduction band has to be more negative than the reduction potential of H^+/H_2 (0 V vs NHE).

1.2. The processes of photocatalytic hydrogen evolution

Figure 4 shows the processes in the photocatalytic generation of hydrogen [15]. They include the absorption of light by the photocatalyst, generation of excited charges (electrons and holes), separation of excited charges, recombination of the excited charges, and transfer of excited charges to water or other molecules. The final generation of hydrogen from the semiconductor photocatalyst system can be affected by all of these processes.

The amount of excited electrons in the water/photocatalyst interface mainly determines the total amount of hydrogen generated in reducing water. Obviously, for maximizing the efficiency of the hydrogen generation of the photocatalyst system, any other processes that consume excited electrons should be avoided. Thus, for the charge-generation process, the reflection or scattering of light by the photocatalyst should be minimized, and the semiconductor photocatalyst should have a low band gap to absorb as much light as possible. Then, the semiconductor photocatalyst should generate excited charges using the absorbed photons, instead of generating phonons or heat.

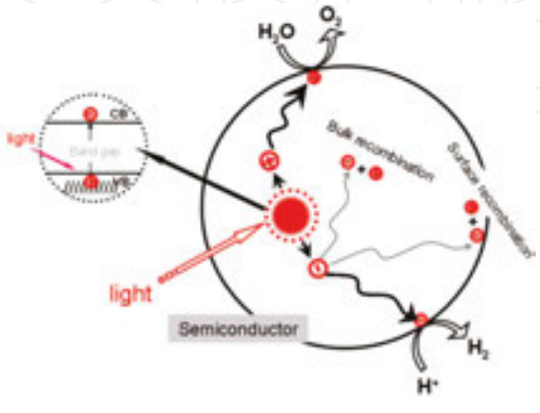

Figure 4. Processes in photocatalytic water splitting. Reprinted with permission from ref [15]. Copyright 1995 American Chemical Society.

After excited charges are created in the semiconductor photocatalyst, charge separation/migration and recombination processes are two important competitive processes [15]. The separation of excited electrons and holes may need to overcome an energy barrier. Charge is separated and migrated to the surface of photocatalyst ready for the desired chemical reaction. These processes are beneficial for hydrogen generation through water splitting. However, charge recombination will reduce the efficiency of water splitting since it reduces the amount of charge. It is important for photocatalytic hydrogen generation through water splitting to include efficient charge separation and fast charge transport for avoiding any bulk/surface charge recombination. Any method beneficial to the charge separation and transport should be applied such as design of heterojunction and use of high performance semiconductor materials (photoconductive).

So two keys should be considered to develop a suitable efficiency semiconductor for the visible-light-driven photocatalytic splitting of water into H_2 and/or O_2. Firstly, for harvest visible light and possess the correct band structure, a photocatalyst should have a sufficiently narrow band gap (1.23 eV< Eg < 3.0 eV). Secondly, to avoid bulk/surface electron/hole recombination, photoinduced charges in the photocatalyst should be separated efficiently. In addition, the electron/hole must migrate to the photocatalyst surface for hydrogen and/or oxygen evolution. In summary, the proper photocatalyst with correct band structure and with economical and highly efficient photocatalytic systems for light-to-hydrogen energy conversion should be constructed.

1.3. Modifying the electronic band structure for visible-light harvesting

To develop photocatalyst using visible-light irradiation, prophase studies were carried out on some narrow band gap semiconductors such as CdS [16] and WO_3[17, 18]. However, the serious photocorrosion of CdS [19] and the relatively positive conduction band of WO_3 proved dissatisfactory for hydrogen production [20] and created major impediments for visible-light-driven water splitting. Some studies were carried out to improve the photocatalytic stability of CdS, [21–24] and others used WO_3 as the photoelectrode in the photoelectrochemical cell for water splitting [25–27]. To overcome these disadvantages, many efforts have been made to develop new visible-light-driven photocatalysts with high water-splitting activities [21–27]. Several common approaches have been adopted in order to enhance the performance of visible-light active of photocatalysts for water splitting, which based on numerous experimental results from the past 20 years. These approaches were shown as follows: (1) developing novel single-phase Vis-active photocatalysts through band gap engineering; (2) dye sensitization to make UV-light-active photocatalysts harvest visible light; (3) developing solid solutions to control the band structure; and (4) metal or/and nonmetal ions doping for band gap narrowing.

In the method of metal or/and nonmetal ions doping for band gap narrowing, one of the most effective ways to develop visible-light driven photocatalysts is to create impurity levels in the forbidden band through nonmetal ion doping. It has been widely used to narrow the band gap and improve the visible-light-driven photocatalytic activity. Nonmetal-ion dopants are less likely to form donor levels just like metal-ion dopants in the forbidden band but instead shift

http://dx.doi.org/10.5772/63487

the valence band edge upward. **Figure 5** shows a narrowing of band gap. The technology of nonmetal-ion doping has been widely used to modify some UV-light-active oxide photocatalysts, such as Ti-based oxides [28–30], Ta-based oxides [31–34], Zr-based oxides [35, 36], and Nb-based oxides [37, 38]. The boron doping has been used to modify 3C-SiC nanowires for effective visible-light-driven photocatalytic activity in our recent work (B-doped 3C-SiC nanowires) [39].

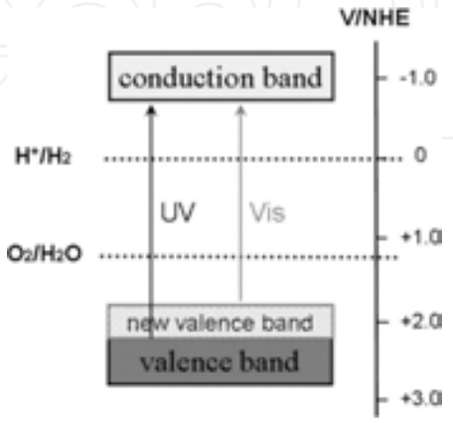

Figure 5. New valence band formation by doping of nonmetal ions [11].

Another promising method for controlling photocatalyst band structure is the formation of solid solutions between wide and narrow band gap semiconductors such as doping. According to this method, varying the ratio of the compositions can control the band gap and position. **Figure 6** shows the controllable band formation by making a solid solution. This method contain (oxy)sulfide solid solutions [40–42], oxide solid solutions [43, 44], and oxynitride solid solutions [45–48]. The way of oxynitride solid solutions were used in our recent work (TiOxNy/TiN) [49].

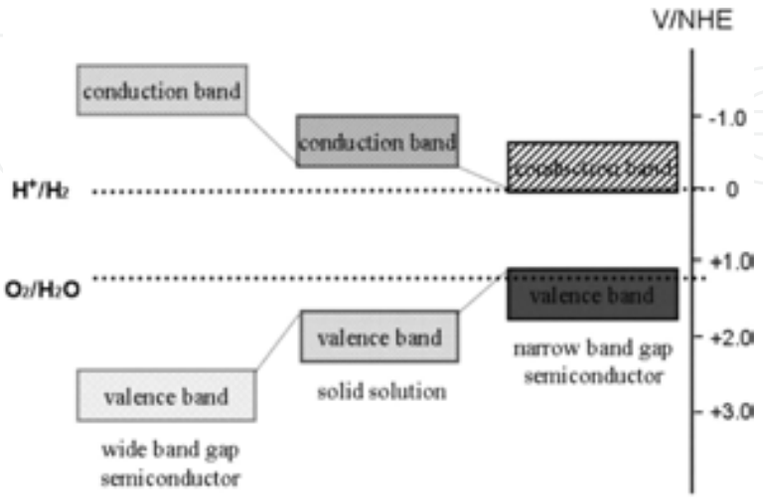

Figure 6. Band structure controlled by making a solid solution [11].

1.4. Efficient photogenerated charge separation

When visible-light-driven photocatalysts with proper band structures are synthesized and charges are excited, the photogenerated charge separation is another key factor strongly affecting the efficiency of the photocatalytic water-splitting process. Clearly, to avoid bulk/surface charge recombination and transfer to the separated active sites on the surface of the photocatalysts, the utilization rate of the photogenerated charges can be improved and high photocatalytic water-splitting activities can be obtained. On the basis of numerous experimental results and theoretical research results from the past decades, several common approaches have been adopted in order to make efficient photogenerated charge separation: (1) cocatalyst loading; (2) semiconductor combinations; (3) modification of crystal structure and morphology.

Transition metals, especially the noble metals, are widely used as effective cocatalysts for photocatalytic water splitting. Taking Pt as an example, **Figure 7** shows the processes of charge transfer between cocatalyst and host photocatalyst. Since the Fermi energy level of noble metal is always lower than that of the semiconductor photocatalyst, the photogenerated electrons migrate to the surface of the host photocatalyst and are entrapped by the noble metal cocatalyst after the surface of the photocatalyst is loaded with the noble metal. Meanwhile, the photogenerated holes migrate to the surface of host photocatalyst. So the photogenerated electrons and holes can be separated efficiently. Subsequently, in the photocatalytic reaction, the separated electrons and holes are involved in the reaction as the reducer and oxidizer, respectively. Overall, the cocatalysts are extremely important. It improves the overall photocatalytic activity of the water splitting because it helps to promote charge separation, which in return reduces both bulk and surface electron/hole recombination. It also accelerates the surface chemical reaction by inhibiting backward reaction. As one of the noble metals, Pt has been widely used as the cocatalyst in photocatalytic water splitting over many different kinds of semiconductors: oxides [50–52], (oxy)sulfides [53–56], and (oxy)nitrides [57–59]. All have been shown to greatly enhance the photocatalytic activity for hydrogen evolution.

The semiconductor combination approach has been shown to be another effective method for improving photocatalytic activity through better photogenerated charge separation with a formation of a heterojunction structure. As shown in **Figure 8**, the staggered band gap type is the most suitable for photocatalytic applications. In this type, the two semiconductors construct a heterostructure on the basis of the matching band potentials. Holes will transfer to the VB of semiconductor-A from semiconductor-B, in which the VB level of semiconductor-A is higher than semiconductor-B. Electrons will transfer to the CB of semiconductor-B from semiconductor-A, in which the CB level of semiconductor-A is higher than semiconductor-B. So the internal field can promote the separation and migration of photogenerated carriers and reduce the recombination of electron–hole. As a result, a mass of holes accumulate on the surface of semiconductor-A and a mass of electrons accumulate on the surface of semiconductor-B. These carriers will participate in photoredox reaction and thus the reaction can be enhanced greatly.

http://dx.doi.org/10.5772/63487

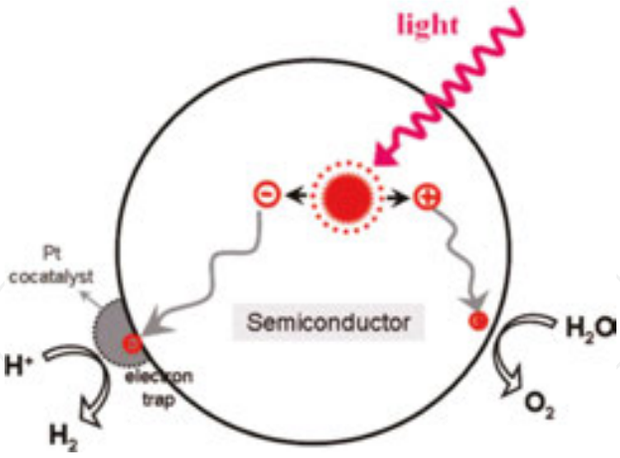

Figure 7. Processes of charge transfer between host photocatalyst and cocatalyst, taking Pt as the example of cocatalyst [11].

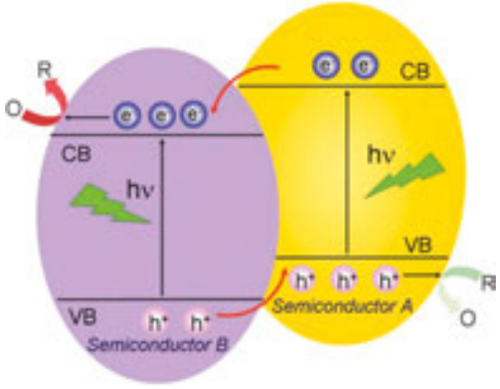

Figure 8. Schematic diagram showing the energy band structure and electron-hole pair separation in the heterojunction [60].

In general, the crystal structural features of the materials, such as crystallinity, defects, and any crystal structure distortion, can strongly affect the charge separation and transfer of photogenerated electrons and holes. Additionally, the morphology of the materials is also important. For example, it includes particle size, surface area, surface structure, and active reaction sites. Thus, on the basis of numerous experimental results and theoretical research results from the past decades, both the modification of crystal structure and morphology of the photocatalysts have been adopted in order to improve efficient charge separation. This has had great success in the enhancement of photocatalytic activity for water splitting.

For crystal structure, it has been well demonstrated that the crystal structure of TiO_2 plays a significant role in photocatalysis. In photocatalysis, for pure-phase TiO_2, the anatase phase was considered to be more active than the rutile phase [61, 62].

It is well-known that particle size is a crucial factor in the dynamics of electron/hole recombination (including bulk recombination and surface recombination) processes, especially in

semiconductor nanomaterials, and that the movement of electrons and holes is primarily governed by the well-known quantum confinement [63]. Generally, when the particle size of photocatalysts decreases, its efficiency will increase in photocatalysis [64–67]. Moreover, reduction in particle size could also lead to a larger surface area and increase the available surface active sites [68, 69]. Lee *et al.* reported that the smaller particle size and higher surface area of $NaTaO_3$ led to higher photocatalytic performance in water splitting [69]. Sathish *et al.* [70] found that CdS nanoparticles showed a higher efficiency of photocatalysis compared to bulk CdS. This result indicated the fact that smaller particle size can increase the performance of a photocatalyst. However, when particle size of the nanocrystalline semiconductor becomes extremely small, this in return can offset the benefits of the ultrahigh surface area of the nanocrystalline particles [71, 72]. So for higher efficiency, the photocatalyst should have the proper size.

Two-dimensional (2D) nanostructures such as nanobelts [73, 74], nanosheets [75, 76], and nanoplates [77, 78] also favor the transfer of electrons and holes generated inside the crystal to the surface and promote charge separation [79–81]. Under identical conditions, Sun *et al*. found that ZnO nanobelt arrays was better than that found for ZnO film or the rod-/comb-like ZnO nanostructures for the photocatalytic properties [73]. Self-assembly of nanoscale building blocks into three dimensional (3D) complex structures is another research hot spot in photocatalysis [82–85]. Song and Gao found that hollow NiO microspheres showed a significantly more enhanced photocatalytic activity than NiO rods [86].

There are two main approaches to enhance the visible-light-driven activity of photocatalysts for developing more efficient that. One is the promotion of the photogenerated charge separation. The other is to narrow the band gaps to harvest visible light in the longer-wavelength regions. Therefore many factors which determine the photocatalytic activity are needed to be applied in one material, such as morphology, structure and crystallinity, chemical composition, surface states, and electronic properties.

Titanium nitride (TiN) is an Fm3m cubic crystal containing both covalent and metallic bonds. It has a narrow energy band gap (0.80 eV) and good electrical conductivity, which are beneficial to photocatalytic H_2 production. However, since the rapid recombination between photoelectrons and holes, its application as a photocatalyst is limited. The inherently high defect density of TiN and unfavorable band position for hydrogen reduction led to the rapid recombination of photoelectrons and holes. 3C-SiC is an important semiconductor with suitable band gap (2.3–3.3 eV) and excellent properties, such as high thermal conductivity, high mechanical strength, and high chemical stability, especially the environmentally friendly property. However, SiC as a photocatalyst does not draw wide attention due to the high recombination rate of photogenerated electron-hole pairs as well as its surface evolution during 3C-SiC nanoparticles or nanocrystal contacting with water. In our recent work, three methods including ion doping, combination with other semiconductor to form heterojunction, and 3D complex structures are adopted to improve the photocatalytic activity of 3C-SiC and TiN from both theoretical and experimental viewpoint, aiming to extend the application of 3C-SiC and TiN as functional material.

http://dx.doi.org/10.5772/63487

2. Theoretical calculations

Band gap engineering is a significant and new approach, which can modify the band structure of semiconductor. In band gap engineering, solid solution, semiconductor sensitization, and ion doping are the most common ways. What's more, theoretical calculation based on first-principle calculations can provide an efficient way to identify a candidate and suggest useful processing and production conditions.

Plane-wave pseudo-potential with Cambridge Serial Total Energy Package (CASTEP) code is adopted in the first-principle calculations. The geometry structure is optimized by using the Broyden-Fletcher-Goldfarb-Shanno (BFGS) [87]. **Table 1** lists all the calculation conditions. The self-consistent field is set to 1×10^{-6} eV/ atom. In the calculation for the DFT exchange-correlation function, the generalized gradient approximation (GGA) [88, 89]is adopted, as specified by Perdew and Wang [90]. The density mixing option is chosen in the electronic minimization method [91].

Task: Geometry optimization			**Energy**
Functional	GGA PW91		LDA CA-PZ [92, 93]
Minimizer	Fine quality		-
	Energy:	1.0e-5 eV/atom	-
	Max force:	0.03 eV/	-
	Max stress:	0.05 GPa	-
	Max displacement:	0.001 Å	-
Algorithm	BFGS:	Use line search	-
Stress	0 for all		-
Energy cutoff	700 eV		700 eV
SCF tolerance	$1.0*10^{-6}$eV/atom		$1.0*10^{-6}$eV/atom
Pseudopotentials	Ultrasoft [94]		Norm-conserving [95]
FFT grid density	Fine quality		Standard
Finite basis correction	Smart		Smart
Electronic minimizer	Density mixing		Density mixing
Orbital occupancy	Fixed		Fixed
k point quality	Fine quality		Fine quality
Band structure	Unchecked		Checked Fine quality k point set
Density of states	Unchecked		Checked Medium quality k point set

Table 1. Calculation conditions for geometry optimization and energy task.

2.1. B-doped 3C-SiC nanowires with finned microstructure

3C-SiC with zinc blende structure is shown in **Figure 9(a)**, and its lattice constant is a=b=c=0.4341 nm. The optimized models are shown in **Figure 9(a)–(d)**, where Si in the symmetrical positions has been substituted by B [96, 97]. The k-point set mesh parameters are chosen to be fine quality in the Brillouin zone for B-doped 3C-SiC ($Si_{31}BC_{32}$, $Si_{15}BC_{16}$, and Si_7BC_8) corresponding to B concentration about 14.3 at%, 6.7 at%, and 3.2 at% respectively.

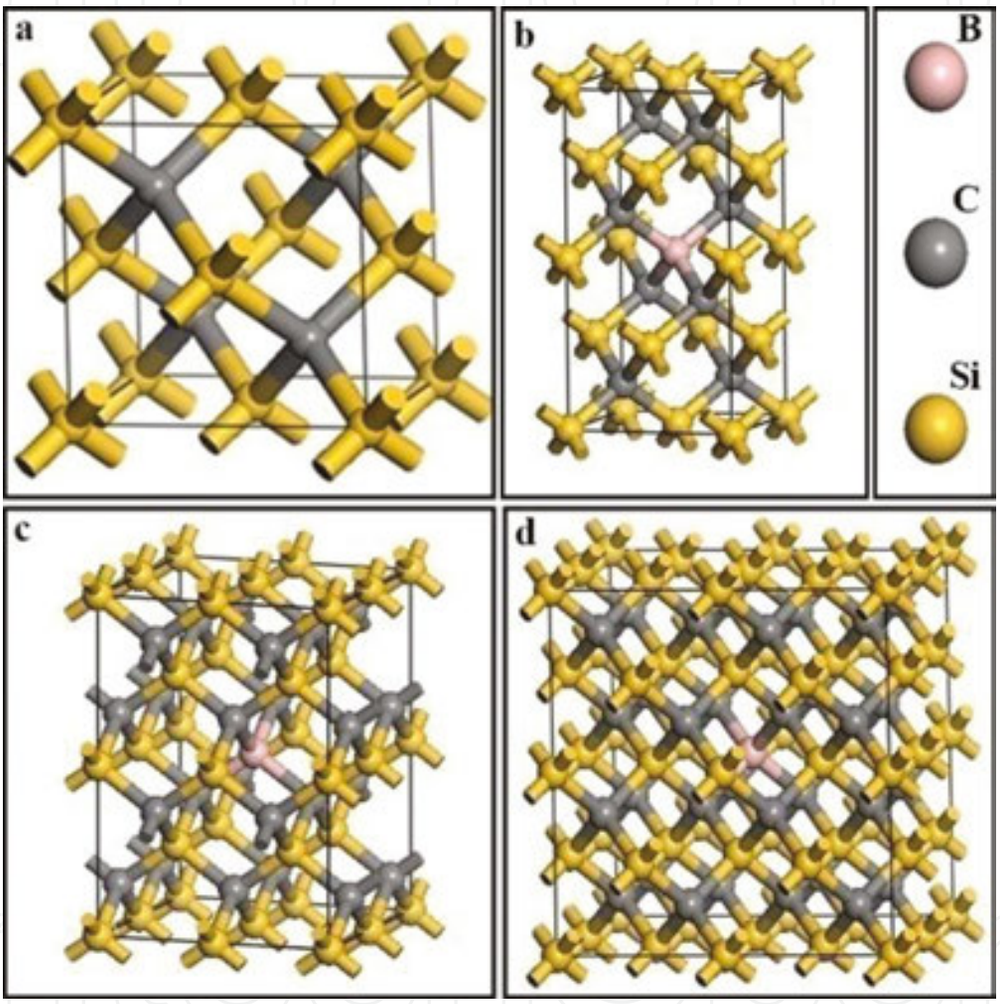

Figure 9. Structures of calculation models for SiC and$Si_{n-1}BC_n$ (n=8, 16, 32).

Figure 10 plots the projected density of states (PDOS) of B-doped 3C-SiC with the ratio of B/Si ranging from 0 to 0.143. According to **Figure 10a**, 3C-SiC is indirect semi-conductor, which is in agreement with the reported result [97]. It is changed to direct semiconductor with B being doped (**Figure 10(b–d)**). As shown in **Figure 10e**, the band gaps decrease continuously from 2.341 eV to 1.935 eV with the molar ratio of B/Si increasing from 0 to 0.143. It is well known that material with much smaller band gap tends to lead to photo-corrosion. Dong *et al.* [96] reported B-doped SiC powder for photocatalytic hydrogen evolution under visible light. In their work, when the B/Si molar ratio is 0.05 in B-doped 3C-SiC, it exhibits the highest hydrogen

http://dx.doi.org/10.5772/63487

evolution rate of 7.41 μmolμg^{-1} h^{-1}. Therefore in the experiment, the molar ratio of B/Si is selected as 0.067, i.e. $Si_{15}BC_{16}$.

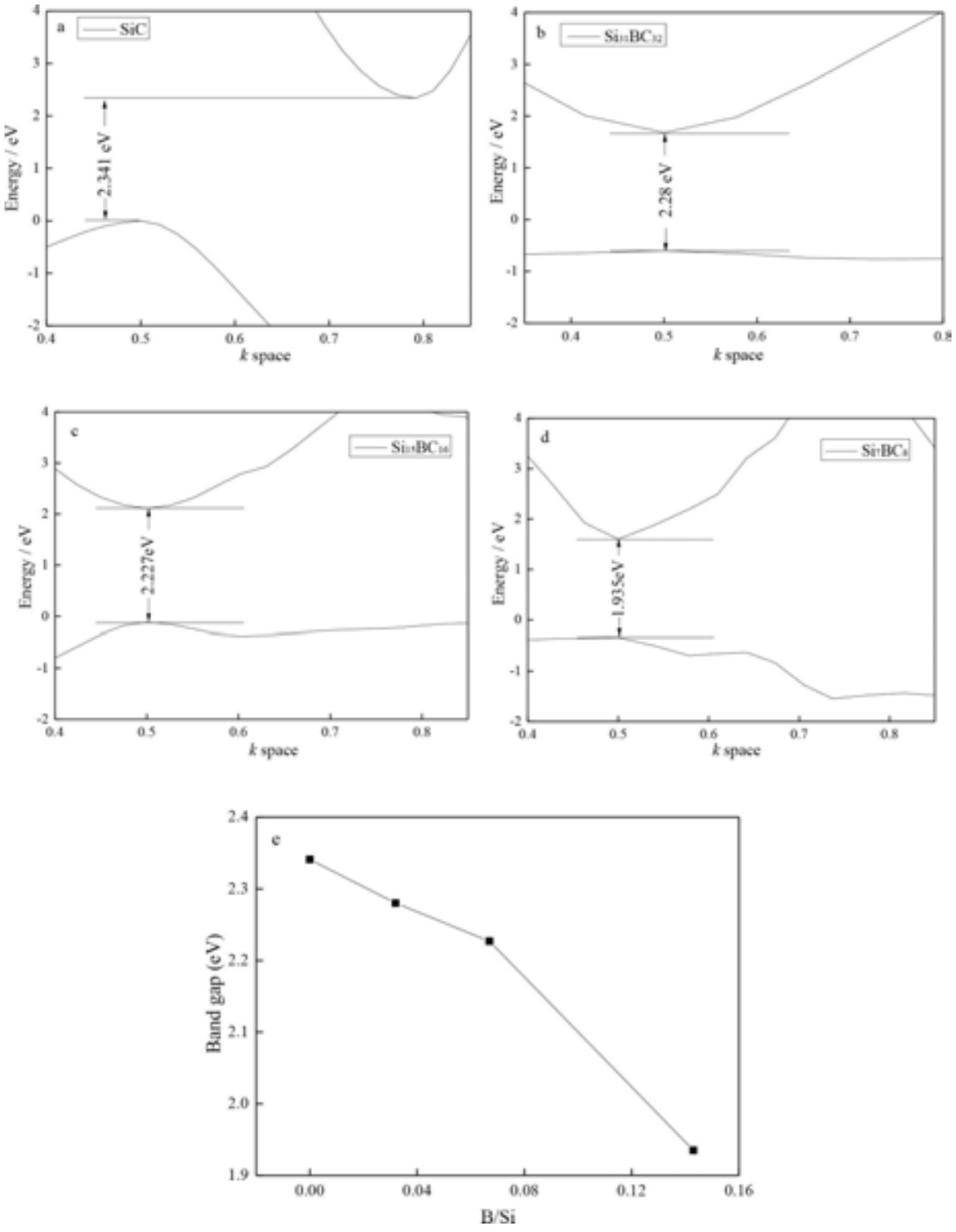

Figure 10. (a)–(d) Calculated PDOS of 3C-SiC and B-doped 3C-SiC including $Si_{31}BC_{32}$, $Si_{15}BC_{16}$ and Si_7BC_8, (e) is the band gap of $Si_{n-1}BC_n$ (n=8, 16, 32).

2.2. TiO_xN_y/TiN heterojunction composite

As for TiN, $TiO_xN_y$is selected as a sensitizer to enhance the photoactivity of TiN. The electronic structures of TiN and TiO_xN_y can be calculated by plane-wave-density function theory (DFT) using the Cambridge Serial Total Energy Package (CASTEP) program package. **Figure 11** shows the optimized simple crystal structures of TiN, Ti_2O_4, and TiO_xN_y with N doping concentration in the range of 0 to 33 mol% ($Ti_{16}O_{31}N$, $Ti_8O_{15}N$, Ti_4O_7N, Ti_2O_3N, and $Ti_2O_2N_2$). O in the symmetrical positions of rutile titanium dioxide (TiO_2) crystal cell has been substituted by N. TiN has a narrow energy band gap (0.80 eV) in **Figure 12a**, which is in consistent with Li's *et al*. work [98]. The calculated band gaps of TiO_xN_y decrease from 3.084 to 0.009 eV with N doping concentration increasing from 0 to 33 mol% (**Figure 12e**).

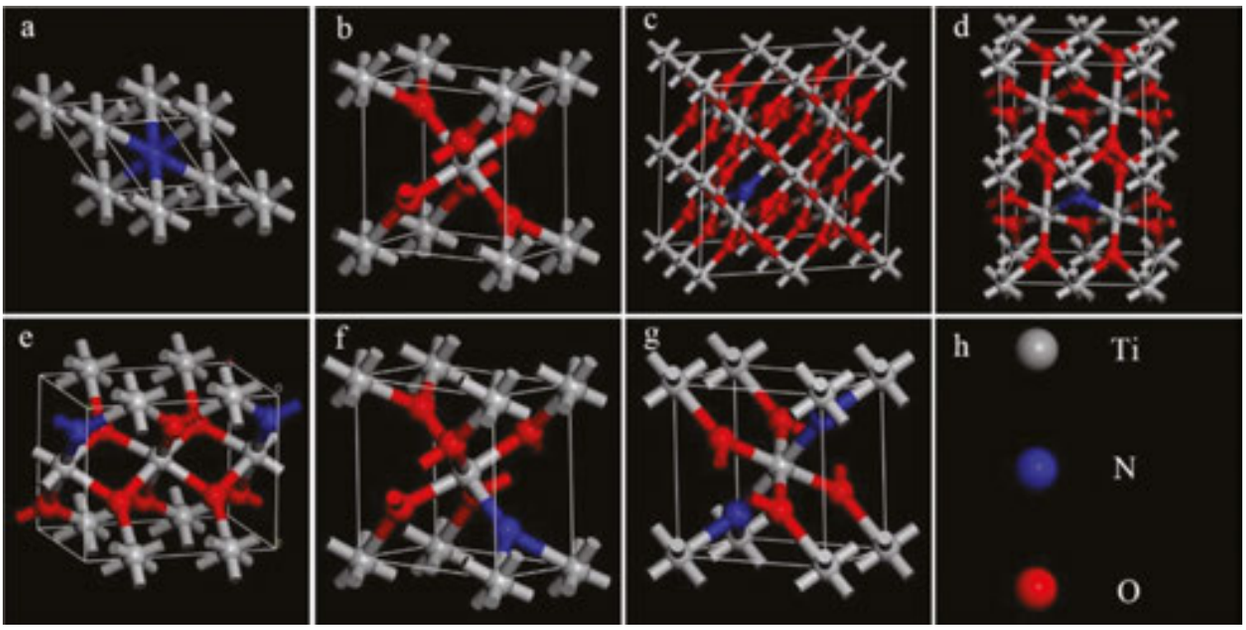

Figure 11. Structures of calculation models for TiO_xN_y.

It can be seen that the band gap of TiO_xN_y is more than 0.8 eV when the doping concentration of N is less than 17 mol% (**Figure 12d** (Ti_2O_3N, 0.918 eV)). Since N introduce new energy band, band gaps of TiO_xN_ychanged with N doping concentration. There is a newly formed energy band introduced by the 2p states of doping N in **Figure 12(c–d)**. From above calculation, TiN combining with TiO_xN_y with proper N doping concentration is expected to form favorable band-edge position, which may be a potential candidate for visible-light responsive photocatalyst.

http://dx.doi.org/10.5772/63487

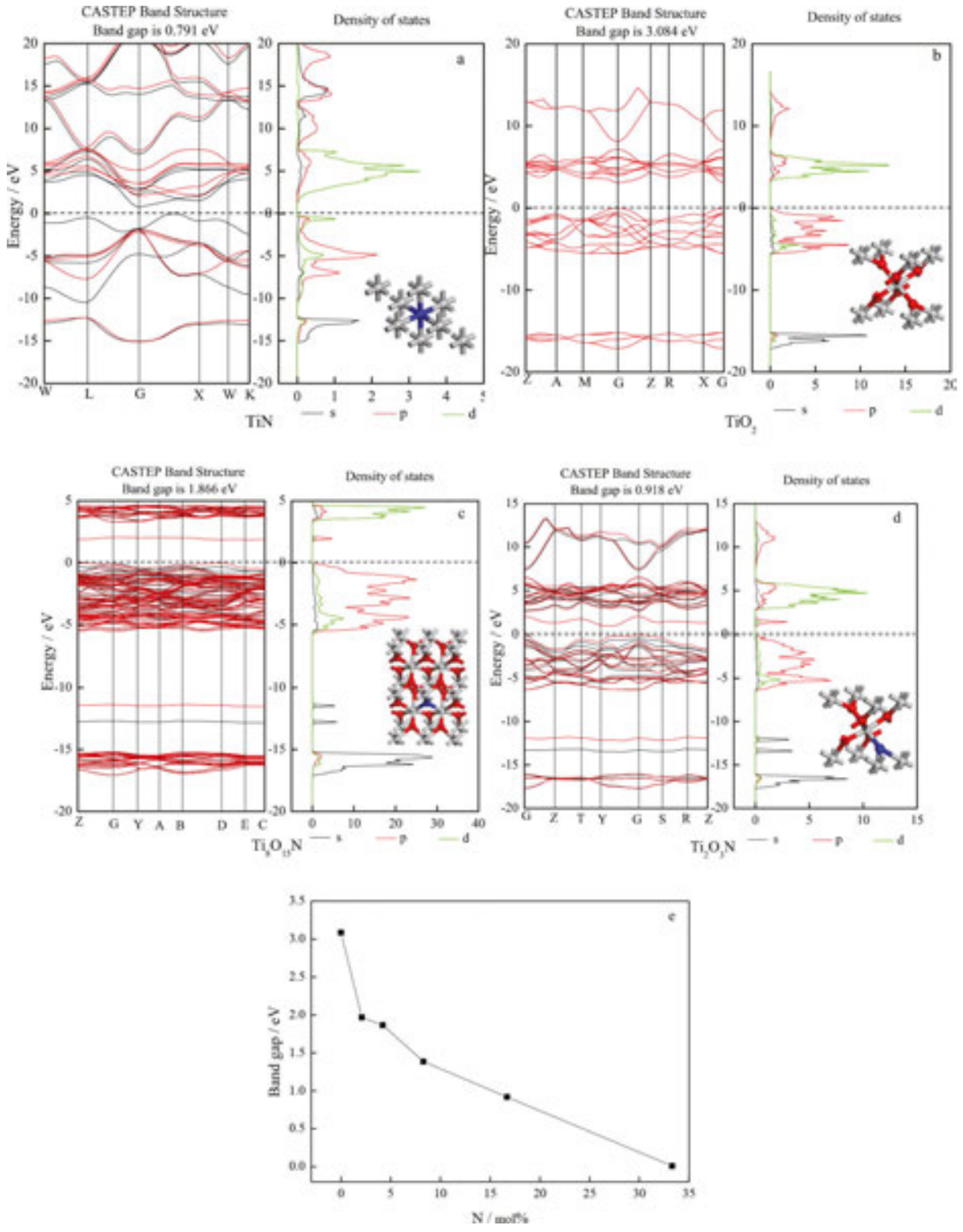

Figure 12. The calculated energy band and density of states of TiN (a), TiO_2 (b), TiO_xN_y (c and d) and the end of band gaps (e). Inset of the crystal structure by the ball-and-stick mode (gray: Ti; red: O; and blue: N).

3. Experimental method for water splitting

3.1. B-doped 3C-SiC nanowires with finned microstructure

Herein a simple synthesis route, i.e. carbonthermal reduction combining the ion doping and morphology modification is adopted in the present work. By controlling the amount of boron doping and the reaction temperature, B-doped 3C-SiC nanowires (NWs) with finned microstructure are obtained. It shows an outstanding activity toward H_2 production as high as 108.4 μmol•h^{-1}, which is about 20 times higher than that of the 3C-SiC nanowires and 2.6 times of the value reported in the literature [99].

3.2. TiO_xN_y/TiN heterojunction composite

TiO_xN_y/TiN heterojunction composite with tunable chamber structures were prepared through reduction and nitridation of organotitania obtained through solvothermal alcoholysis at 900°C for 4 h in partial cracked NH_3. Owing to the low synthesis temperature, TiO_xN_y/TiN duplicates the original structure of the organotitania. It demonstrates an outstanding photocatalytic activity as high as 34.9 μmol•h^{-1}•g^{-1}, which is about 1.5 times higher than the highest value reported in the literature for TiN [98].

4. Results and discussion

4.1. B-doped 3C-SiC nanowires with finned microstructure

4.1.1. Characterization of B-doped 3C-SiC NWs

Figure 13 shows the pattern of X-ray diffraction (XRD) of the B-doped SiC NWs. For comparison, 3C-SiC NWs obtained in our experiment is also investigated. In the two sample, three diffraction peaks at 2θ =35.8°, 60°, and 72° corresponding to cubic SiC (JCPDS card no. 73-1665) both appear suggesting B doping does not change the phase structure of 3C-SiC. However, the characteristic peak of B-doped 3C-SiC shifts towards higher 2θ angle according to the magnification of diffraction peak (111). This change is possibly caused by the substitution of smaller B (0.095 nm) at Si (0.134 nm) [97]. The stacking defects (SF) of SiC were studied by Tateyama *et al.* [100]. The estimation formula was proposed as follows:

$$d_{SF} = \frac{I_{SF}}{I_{(200)}}$$

In the formula, $I_{(200)}$ is the intensity values of (200) peak (41.4°) and $I_{SF}$is the intensity values of SF peak (33.6°). The density of SF in SiC is represented by the ratio value (d_{SF}).As shown in **Figure 13**, the SF peak (red circles) is too weak to calculate the density, which indicates that there are only a few defects in SiC whiskers.

http://dx.doi.org/10.5772/63487

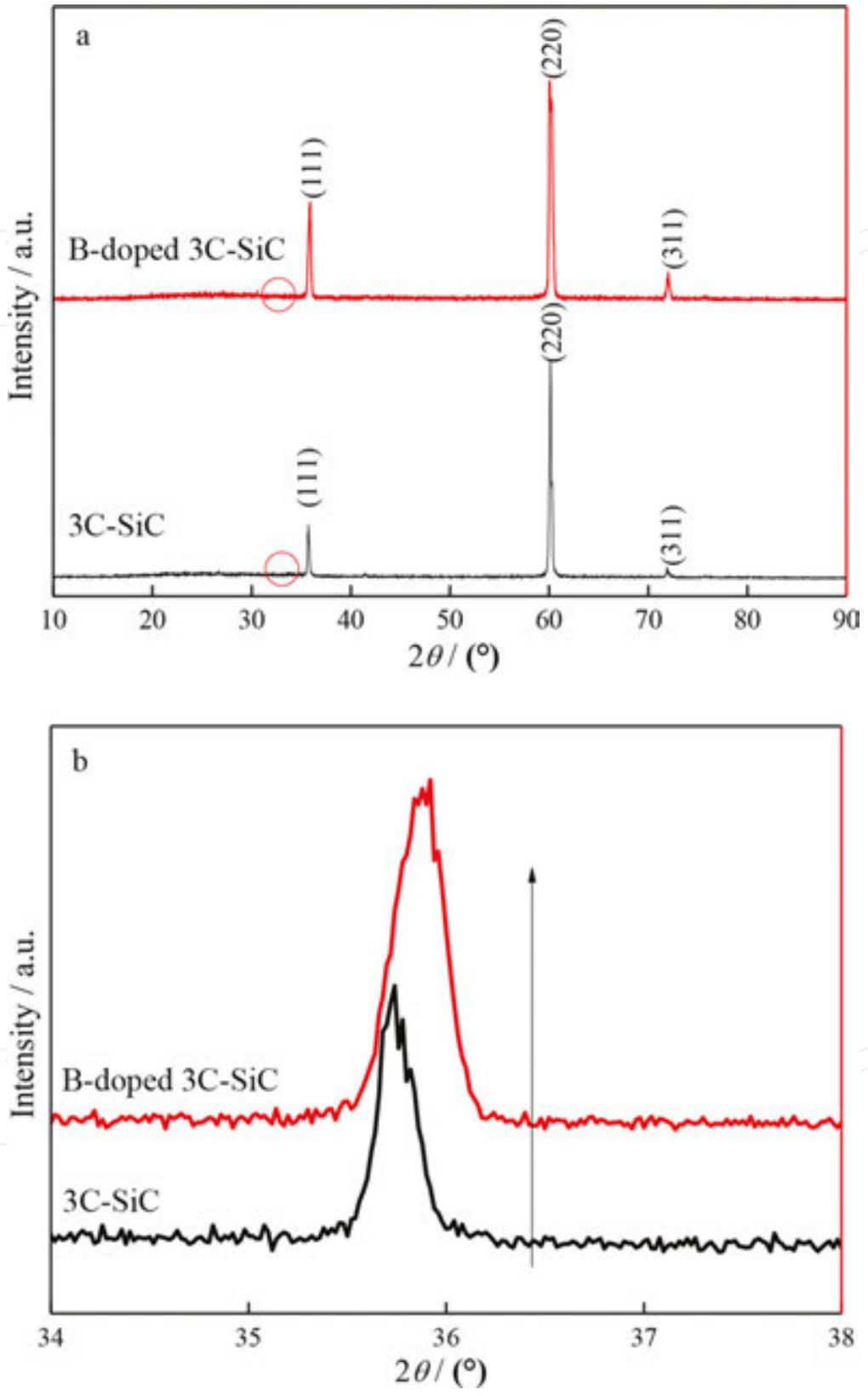

Figure 13. XRD patterns of the as-prepared (a) and the magnification of the diffraction peak (111) (b).

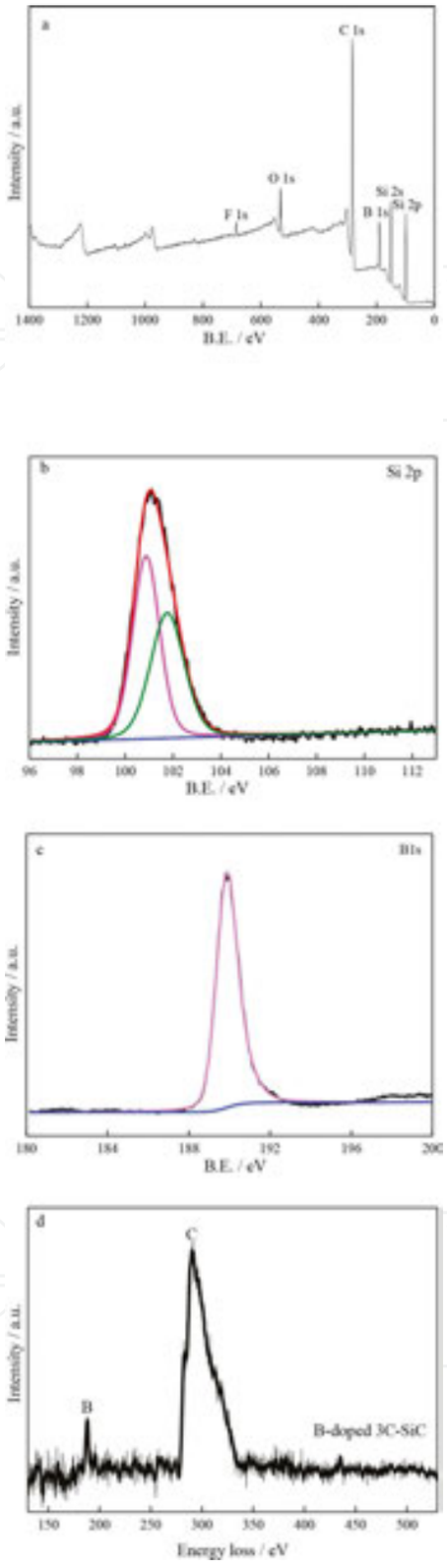

Figure 14. The full spectrum of XPS of B-doped 3C-SiC (a), XPS spectra of (b) Si 2p, (c) B 1s, (d) Electron energy loss spectroscopy (EELS) of B-doped 3C-SiC.

http://dx.doi.org/10.5772/63487

X-ray photoelectron spectroscopy (XPS) is used to characterize B-doped 3C-SiC NWs. The full spectrum of XPS shows the existence of Si, C, B, F, and O in **Figure 14**. Since HF is adopted to treat the surface of sample, F possibly comes from it. **Figure 14b** shows Si 2p fine XPS spectra of the B-doped 3C-SiC NWs sample. From the XPS spectra of Si 2p of B-doped 3C-SiC (**Figure 14b**), the peak centered at 100.7 eV corresponds to Si-C bond in SiC. The peak at 101.8 eV can be assigned to SiOxCy [101]. Two reasons are attributed to the formation of SiOxCy. First is the surface of sample tends to absorb oxygen after treated by HF. Second is SiCxOy is the intermediate product of SiC [101] that is left on the sample. However, the content of SiOxCy is too low to be detected by XRD analysis. **Figure 14c** show B 1s fine XPS spectra of the B-doped 3C-SiC NWs sample.

XPS signals of B 1s can be assigned to the B-C bond in SiC, which are observed at 189.8 eV [101]. The peak at 187.4 eV corresponds to the B-Si bond in SiC and the peak at 193.1 eV corresponds to B-O bond for B_2O_3[102]. In this work, these peaks are not found. This indicates that B atoms incorporate into SiC lattice and substitute Si sites, which are consistent with the reported results [96, 97]. The B/Si molar ratio, as determined by XPS, is 0.066, which is close to the theoretical content of $Si_{15}BC_{16}$. Electron energy loss spectroscopy (EELS) was carried out to further investigate the existence of B element in B-doped 3C-SiC. The peak at 284 eV corresponds to C element and the peak centered at 188 eV corresponds to B element (**Figure 14d**). This further indicates that B-doped 3C-SiC is synthesized in the experiment.

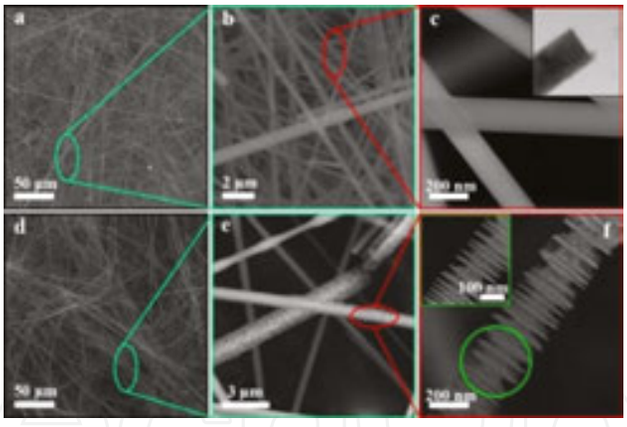

Figure 15. SEM images of the as-prepared 3C-SiC (a–c) and B-doped 3C-SiC (b–d).

SEM and TEM techniques are used to reveal the morphology and microstructure of the as-prepared samples. **Figure 15** show SEM images of the synthesized 3C-SiC NWs. **Figure 15a** and d show the overall looks of the 3C-SiC NWs and B-doped 3C-SiC NWs at low magnification, which indicate that the majority of the nanowires can be described as long and straight filaments with the length up to several mm. As shown in SEM at higher magnification (**Figure 15b**), the typical morphology of 3C-SiC NWs possess smooth surface and the average diameter is about 80 nm. The whisker has a homogeneous crystalline structure with fringes spacing at 2.51 Å as shown in **Figure 16b**, which is characteristic of 3C-SiC. By comparison, the morphology of B-doped 3C-SiC NWs changes a lot. The typical morphology of the B-

doped 3C-SiC NWs is finned nanowires as shown in the magnified images (**Figure 15e** and **f**). It is composed of inner core stems and outer fins. **Figure 16c** and d show TEM images of typical finned like B-doped 3C-SiC NWs. The thickness of the fins is 10–20 nm. The diameter of the inner core stems is about 80 nm and the fins is about 100–200 nm. The lattice spacing of a fin is 2.50 Å as shown in **Figure 16e**. From SAED pattern of the fin (the inset of **Figure 16e**), it is single crystal. The HRTEM image reveals that the lattice spacing of the nanowire is also 2.50 Å in **Figure 16f**. It is caused by substitution of smaller B (0.095 nm) at Si (0.134 nm) and leads to the distortion of the lattice.

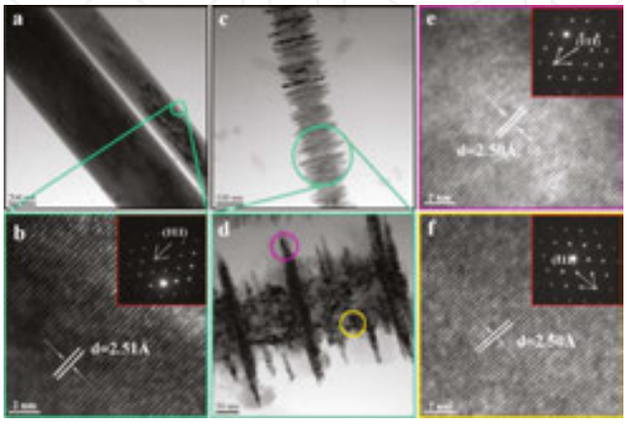

Figure 16. TEM images of the as-prepared 3C-SiC (a–b) and B-doped 3C-SiC (c–f).

For the formation of hierarchical nanostructures, two growth mechanisms are put forward [103–105]. Self-assembly of nanobuilding blocks is one formation mechanism, wherein blocks include balls, wires, and platelets [105]. Inner 1D core structures and then the epitaxial growth of secondary branches is another formation mechanism [103, 104]. As shown in **Figure 17a**, some SiC NWs possessing rough and uneven surface are found in this work. Therefore the formation of finned 3C-SiC NWs cloud be the two-step epitaxial growth process.

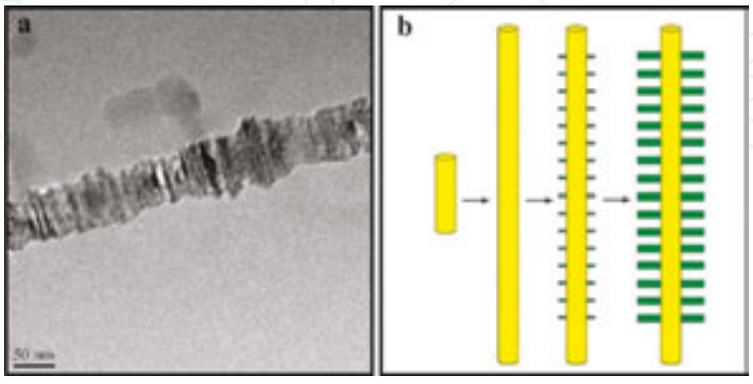

Figure 17. (a). The rough and uneven surface of SiC core stem caused by the stacking faults. (b). Schematic illustration of a possible SiC nanoarchitecture growth process.

In the experiment, the possible reactions take place as following:

http://dx.doi.org/10.5772/63487

$$SiO_2(s) + C(s) \rightarrow SiO(g) + CO(g) \quad (1)$$

$$B_2O_3(g) \rightarrow 2B(s) + 3/2O_2(g) \quad (2)$$

$$15SiO(g) + B(s) + 47CO(g) \rightarrow Si_{15}BC_{16}(s) + 31CO_2(g) \quad (3)$$

$$C(s) + CO_2(g) \rightarrow 2CO(g) \quad (4)$$

SiO vapor plays an important role during the synthesis of 3C-SiC whiskers [105]. The formation of B according to **Equation (2)** makes B doping possible and thus is a key step. The standard reaction Gibbs energies of **Equation (2)** are 767412.5 J•mol^{-1}using the database of FactSage 6.4. In our experiment, the partial pressure of O_2 is controlled to be 2.6×10^{-12} Pa, which is verified by mass spectrometry. The vapor pressure of B_2O_3 is 152 Pa at 1500°C according to the Speiser's [106] result as following:

$$\lg p_{B_2O_3}(\text{atm.}) = -(77600/4.575\ T) + 6.742$$

Therefore, the reaction Gibbs energy of **Equation (2)** can be calculated as follows:

$$\Delta rG_{1773} = \Delta rG^{\theta} + RTlnJ$$

$$= 767412.5 + 8.314\times1773\ln\frac{P_{O_2}^{\frac{3}{2}}}{P_{B_2O_3}}$$

$$= 767412.5 + 8.314\times1773\ln\frac{(2.57\times10^{-17})^{\frac{3}{2}}}{1.52\times10^{-3}}$$

$$= 58715.5\ \text{J}\cdot\text{mol}^{1}$$

where *J* is the reaction constant of **Equation (2)** at 1500°C. Therefore the reaction Gibbs energy of **Equation (2)** is calculated to be −58715.5 J/mol, indicating that the reaction can take place under the experimental condition.

Owing to the high temperature, the formation of inner 1D core stem is the first step in a two-step epitaxial growth process. When reaction between CO, B, and SiO occurs, the B-doped SiC($Si_{15}BC_{16}$) will be formed (**Equation (3)**). CO_2 reacts with C to form CO according to **Equation (4)**, which causes CO to remain at a supersaturated level and thus **Equation (3)** continues to proceed. This leads B-doped SiC($Si_{15}BC_{16}$) to precipitate as nuclei and grow along the (111) direction due to the lowest surface energy to form the core stem B-doped SiC ($Si_{15}BC_{16}$) nanowires. Since SiC NWs have more defects after B doping, the nanowires possess

rough and uneven surface (as shown in **Figure 17a**). When the temperature is decreased and the amount of SiO becomes less, the growth rate of B-doped SiC will become lower. Since the energy for nucleating SiC on B-doped SiC core stems is far lower than that on the other places, the newly formed B-doped SiC tends to grow on that. Therefore, the fins are formed on the core stems. With time prolonging, B-doped SiC nanowire with finned structure are produced.

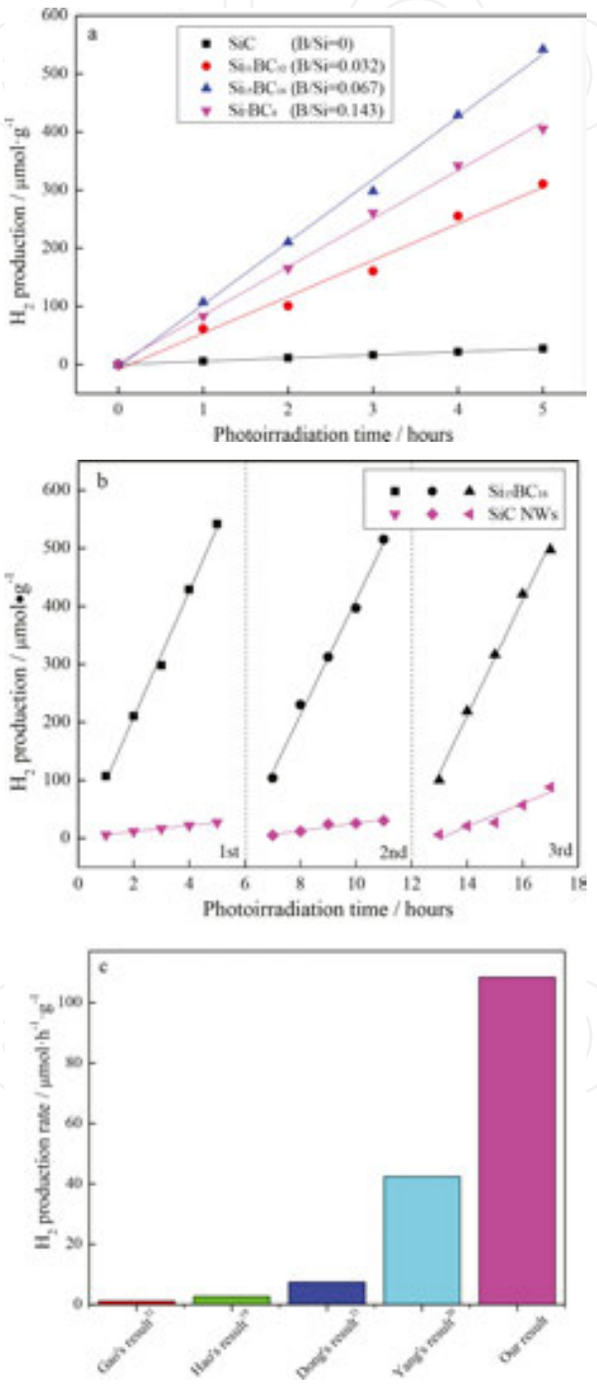

Figure 18. (a). Photocatalytic hydrogen evolution performance over BxSiC. (b). Hydrogen production rates of as-prepared the 3C-SiC NWs and B-doped 3C-SiC NWs. (c). The comparison of Hydrogen production rates.

http://dx.doi.org/10.5772/63487

4.1.2. Water splitting for hydrogen

The 3C-SiC NWs and B-doped 3C-SiC NWs are evaluated under visible-light irradiation for their photocatalytic activities for H_2-production in aqueous suspensions with Na_2S and Na_2SO_3 as sacrificial agents (electron donor). Photocatalytic activities of B-doped SiC with different B/Si ratios are compared in **Figure 18**. B doping significantly affects the photocatalytic activity as shown in Figure 18. The photocatalytic H_2-production rate of sample from high to low is $Si_{15}BC_{16}$ (108.4 μmol•h^{-1}•g^{-1}), Si_7BC_8 (81.0 μmol•h^{-1}•g^{-1}), $Si_{31}BC_{32}$ (62.1 μmol•h^{-1}•g^{-1}), and pure 3C-SiC (5.46 μmol•h^{-1}•g^{-1}).The recycling reaction experiments were carried out to investigate the stability of photocatalytic hydrogen production of 3C-SiC NWs and B-doped 3C-SiC NWs ($Si_{15}BC_{16}$) under visible light irradiation. No decrease in catalytic activity is observed in the recycling reactions as shown in **Figure 18b**. The H_2 production rate for the B-doped 3C-SiC NWs exceeds that of 3C-SiC NWs by more than 20 times. It also exhibits enhanced activity toward H_2 production compared with the recent work as shown in **Figure 18c**. Wang's work group reported SiC fine powder, which can achieve at a value of 1.11 μmol•h^{-1}•g^{-1}[107]. Guo's work group reported modified SiC nanowires, which can achieve at a value of 2.68 μmol•h^{-1}•g^{-1}[108]. And Dong's work group reported boron-doped SiC powder, which can achieve at a value of 7.41 μmol•h^{-1}•g^{-1}[96]. Among these work, the reduced grapheme oxide/SiC showed the larger visible-light-driven photocatalytic hydrogen production done by Yuan's work group to be 42.4 μmol•h^{-1}•g^{-1}[99]. Our result is 108.4 μmol•h^{-1}•g^{-1}, which is 2.6 times higher than that of the reported reduced grapheme oxide/SiC.

In view of the photocatalytic hydrogen production mechanism of B-doped 3C-SiC NWs, first is attributed to the smaller band gaps with B doping as shown in **Figure 10**. It is well know that the positions of the valence band maximum (VBM) and the conduction band minimum (CBM) are critical variables in determining the feasibility of visible-light-driven photocatalytic hydrogen production. As shown in **Figure 19**, it can be seen that the CB and VB potentials (E_{CB} and E_{VB}) of 3C-SiC are E_{CB}=0 eV and E_{VB}= 2.341 eV (**Figure 19a** and **b**). After B doping, the CB and VB potentials (E_{CB} and E_{VB}) are decreased to E_{CB}=−0.4 eV and E_{VB}= 1.827 eV (**Figure 19c** and **d**). Since the mixing of Si 3p and B 2p orbital, the CBM of B-doping 3C-SiC decrease. And since the mixing of C 2s, Si 3s, and B 2p orbital, the VBM decrease. As a result, the CB edge potential of B-doped 3C-SiC is more negative than normal hydrogen electrode (NHE), indicating that photoinduced electrons can easily transfer from B-doped 3C-SiC NWs to H^+ and generate hydrogen. This can also be confirmed by the UV-vis diffusion reflectance spectra (**Figure 20a**). The UV-vis spectra of 3C-SiC NWs shows a strong ultraviolet absorption from 200 to 500 nm (the black line of **Figure 20a**). The red line of **Figure 20a** is the UV-vis spectra of B-doped 3C-SiC NWs, which the absorption edge extends to the visible region (about 800 nm) and the absorption intensity is also enhanced. The band gap of the SiC is calculated using the Kubelka-Munk function [109]. As shown in **Figure 20b**, an intercept value of 2.34 eV for 3C-SiC NWs (the black line) is close to that of the bulk 3C-SiC (2.35 eV). An intercept value of 2.216 eV for B-doped 3C-SiC NWs (the red line) is close to that of the calculated value using DFT.

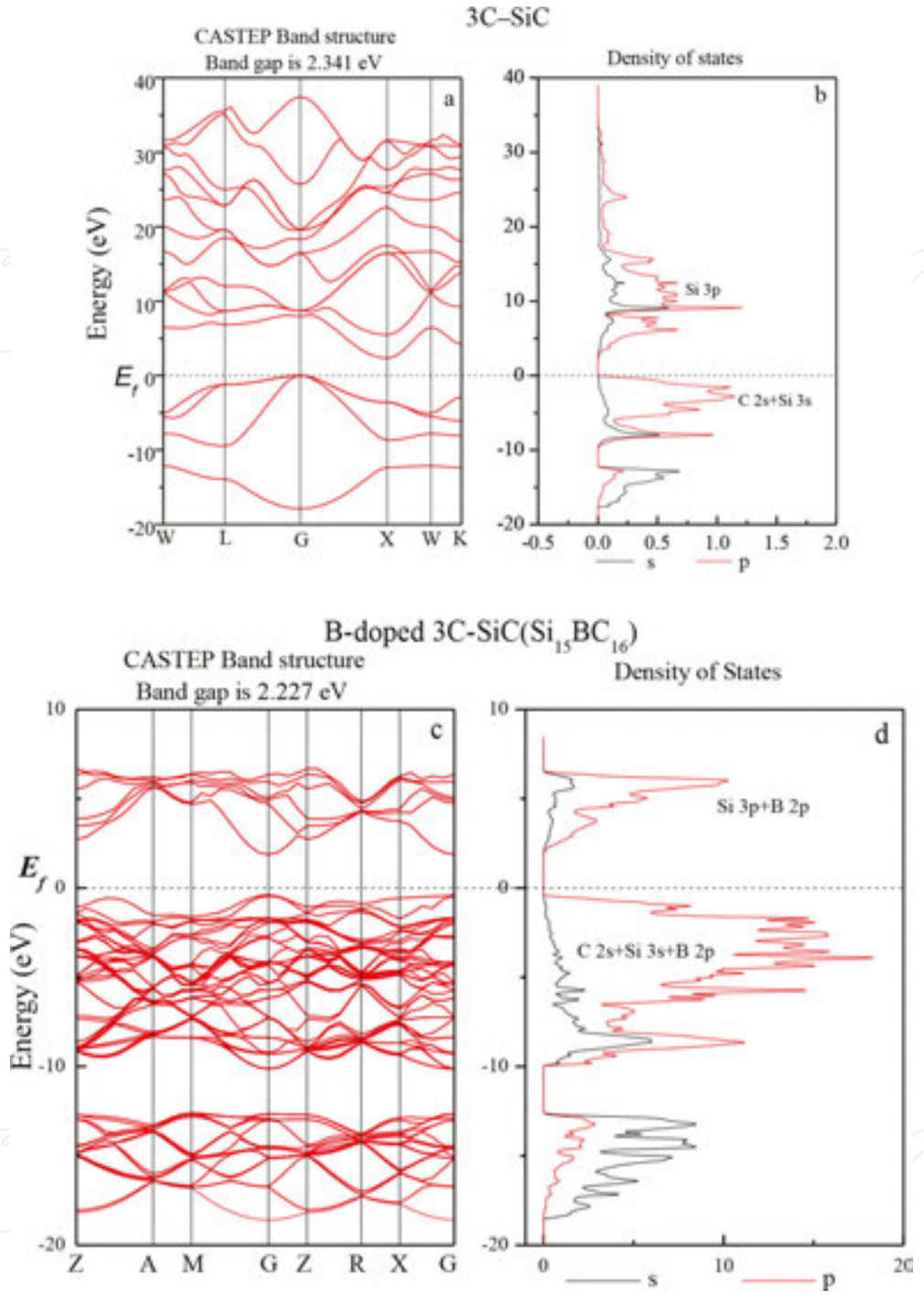

Figure 19. The calculated energy band and density of states (DOS) of pure 3C-SiC (a and b) and B-doped 3C-SiC (c and d).

During the photocatalytic process, the photo generated electron recombination is mainly responsible for the low photocatalysis efficiency. Charge transfer effect can be characterized by PL quenching effect within the sample. After B doping, the PL intensity of 3C-SiC decreases obviously (**Figure 21**). PL is mainly caused by the transitions of electrons to release photons. In this work, electron is transferred instead of transitioning to lower energy level in the B

http://dx.doi.org/10.5772/63487

doping 3C-SiC NWs. Otherwise, as shown in **Figure 13a**, less stacking defects and the special finned like single crystalline nanowires are beneficial to enhance transfer of electron. This makes the charge pathway much smoother. Since the multiple light reflects within the fins of nanowires (inset **Figure 22**) and increases the contacting area with aqueous suspensions, the special finned like morphology also contributes to higher photocatalytic hydrogen production.

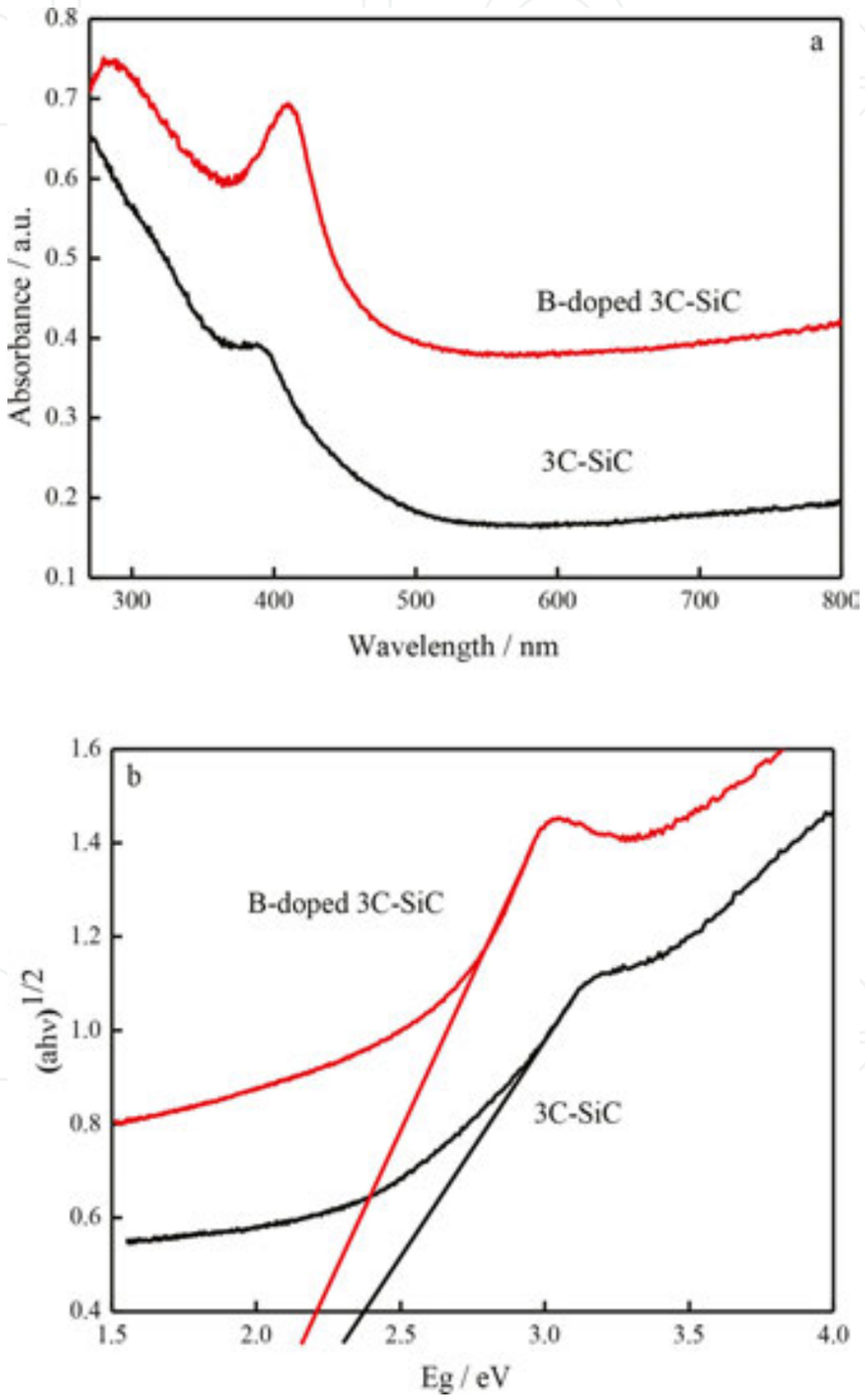

Figure 20. (a) UV-Vis diffusion reflectance spectra. (b) The plots of $(\alpha h\nu)^{1/2}$ versus $h\nu$. The band gap of the samples.

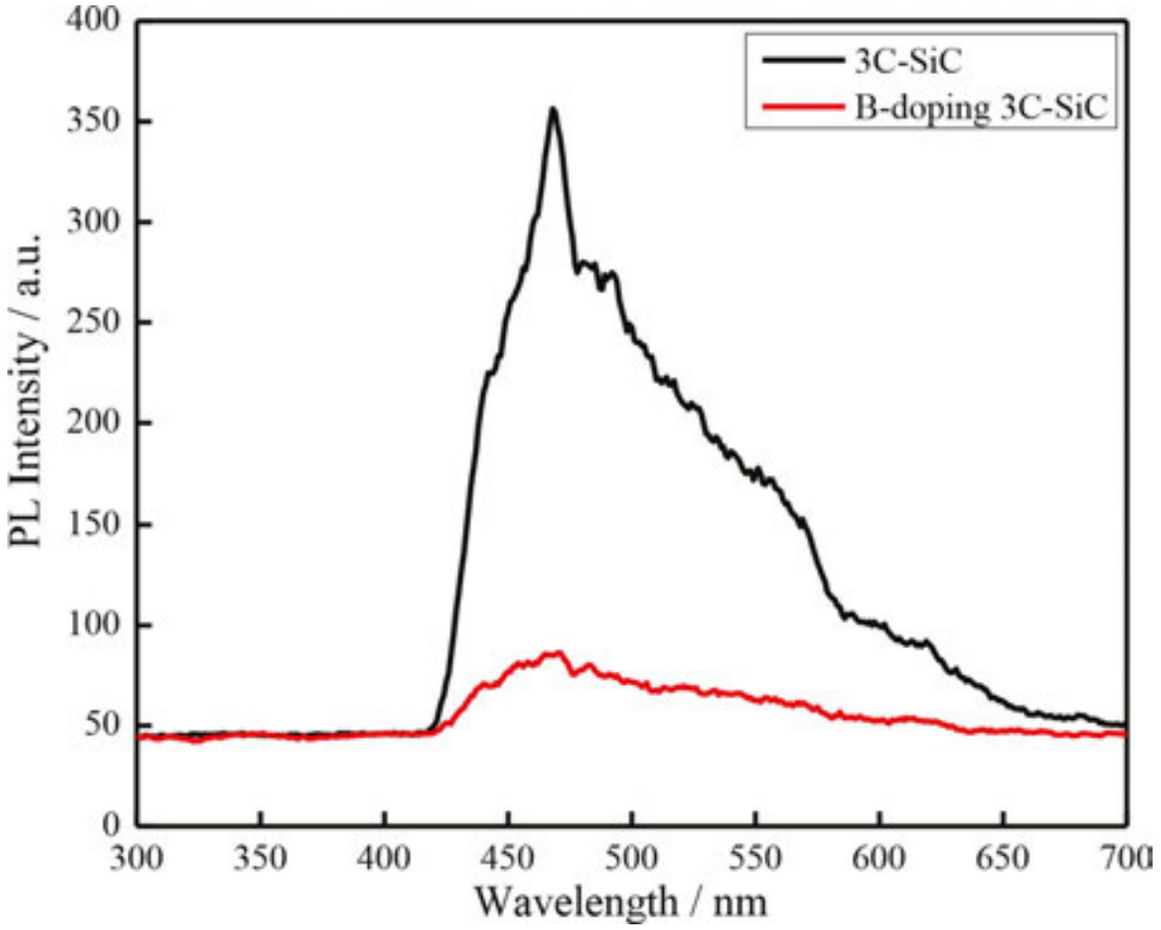

Figure 21. Photoluminescence spectra of 3C-SiC and B-doped 3C-SiC.

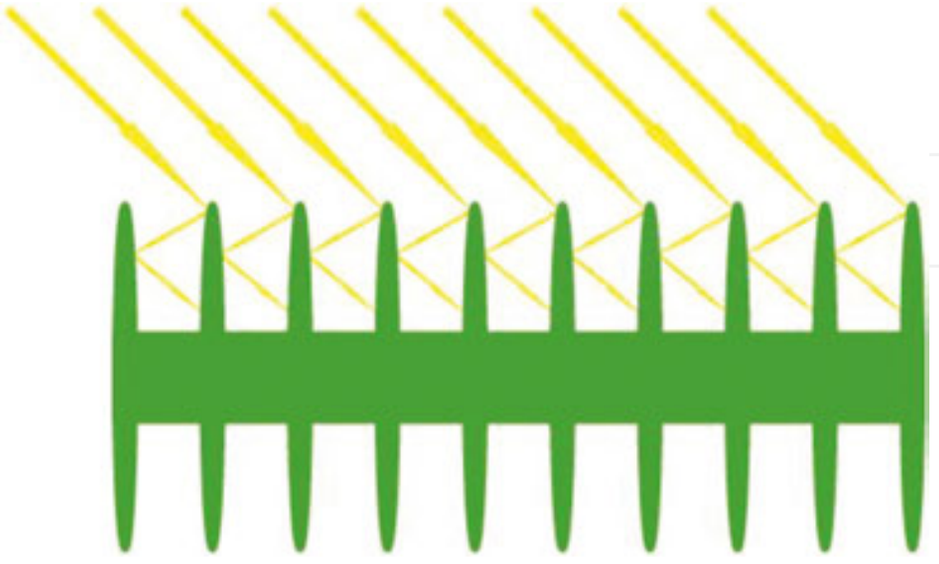

Figure 22. Light reflection models in the B-doped 3C-SiC nanowires.

http://dx.doi.org/10.5772/63487

From above results, using a facile and simple carbothermal reduction of a mixture of low-cost boric oxide powder, gangue and carbon black, finned nanostructure B-doped 3C-SiC NWs were synthesized. The growth process belongs to a two-step epitaxial growth mechanism. Combining the theoretical calculation and experimental result, B substitutes Si during the doping process and possesses smaller band gaps. B-doped 3C-SiC NWs demonstrates an enhanced and stable activity for H_2 production as high as 108.4 μmol•h^{-1}, which is about 20 times of that of 3C-SiC and 2.6 times of the value reported in the literature. It appears that the combined effect of such factors as the single crystal, electronic structures, and the finned like morphology is attributed to the enhanced photocatalytic hydrogen production. This work presents an applicable method to develop various semiconductors with controllable morphology applied in solar energy conversion, gas sensors, and photoluminescence.

4.2. TiO_xN_y/TiN heterojunction composite

4.2.1. Crystal phase analyses

In all the samples, five diffraction peaks at 2θ = 36.90°, 42.86°, 62.24°, 74.61°, and 78.48° corresponding to TiN (PDF 38-1420).As shown in **Figure 23a**, with increasing nitridation temperature, the crystallization degree and purity of TiN increase. The constant *a* increases from 4.216 (800°C) to 4.241 Å (900°C) according to the data of refinement XRD (**Table 2**). And the theoretical value of TiO is 4.180 Å and that of TiO is 4.180 Å [110]. The value of sample is between TiO and TiN, indicating the existence of TiO_xN_y. When the temperature reaches up to 950–1000°C, the constant *a* is calculated to be 4.241Å, which is in consistent with the standard value of TiN (PDF 38-1420 (a=4.241Å)) [111].

Temperature (°C)	800	850	900	950	1000	JCPDS card 38-1420
a (nm)	0.4216	0.4228	0.4237	0.4241	0.4241	0.4241
Grain size (nm)	35.5±1.5	36.1±1.9	37.0±1.6	37.9±1.7	38.5±2.4	

Table 2 .The lattice parameter and grain size of the nitridation products at different temperature with 3 h.

In view of the effect of reaction time, **Figure 23b** shows the XRD patterns of the samples obtained at 900°C for different reaction time at partial cracked NH_3 atmosphere. When the reaction time is 3 h, some small diffraction peaks of TiO_2 still exist. All the characteristic peaks are indexed to be that of TiN with the nitridation time is extended to 4–5 h. **Table 3** shows the refinement of XRD data at 900°C for different time. The constant *a* increases with the reaction time prolonging. When the nitridation time is 4 h, the constant *a* (4.238 Å) is between the theoretical value of TiO (4.180 Å) and TiN (4.241 Å), indicating the existence of TiO_xN_y. From above experiments, the synthesis condition of TiO_xN_y/TiN composite is selected as 900°C and 4 h. Pure TiN can be produced at 1000°C for 3 h.

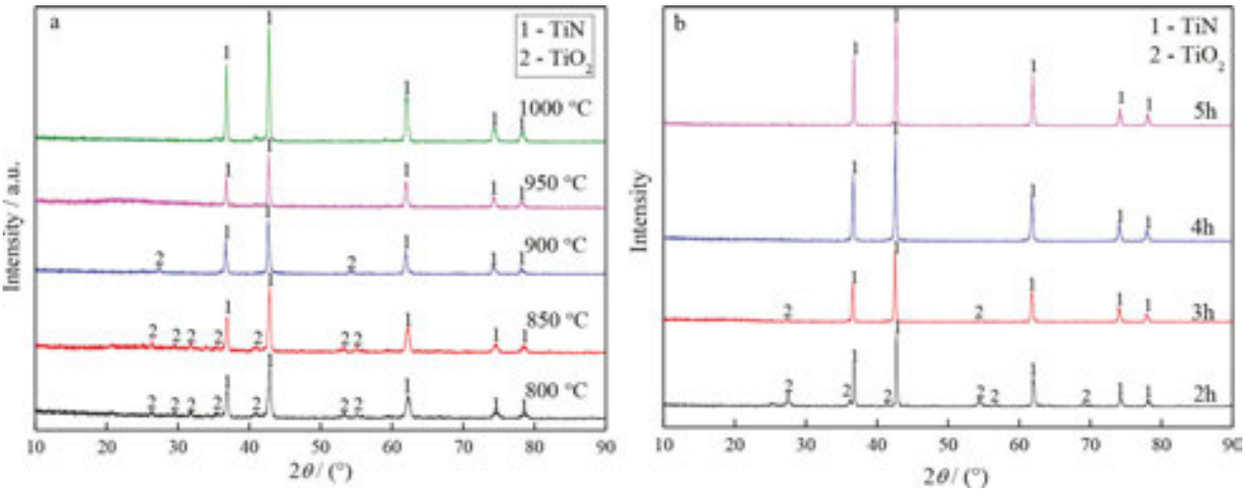

Figure 23. XRD patterns of the obtained yolk-shell TiO_xN_y/TiN composites (a) different temperature for 3 h (b) different time at 900°C.

Time (h)	2	3	4	5	JCPDS card 38-1420
a (nm)	0.4233	0.4236	0.4238	0.4241	0.4241
Grain size (nm)	35.2±1.3	36.8±2.2	37.2±1.4	38.3±0.7	

Table 3. The lattice parameter and grain size of the nitridation products with different time at 900°C.

XPS is adopted to further characterize TiO_xN_y/TiN composite. **Figure 24(a)** shows the full XPS spectrum of the samples obtained at 900°C for 4 h, which indicate the existence of C, N, Ti, and O. **Figure 24(b–d)** show fine XPS spectra of Ti 2p, N 1s, and O 1s. The Ti 2p bands have three groups of peaks, i.e. the typical peaks for TiN (455.3 eV, 457.5 eV, 460.9 eV, and 463.0 eV), the peaks for TiO_xN_y(456.1 eV and 461.7 eV), and the peaks for TiO_2 (459.1 eV and 464.7 eV) (**Figure 24b**) [110–113]. The existence of $TiO_2$is attributed to the reaction of TiN and TiO_xN_y particles with oxygen from air atmosphere. From the XPS spectra of N 1s (**Figure 24c**), the peak at 396.3 eV can be assigned to TiO_xN_y [110, 111, 114]. The peak centered at 397.3 eV corresponds to Ti-N bond in TiN and peak at 399.2 eV corresponds to C=N bond [110]. The absorption of C from the atmosphere led to the existence of C=N. From the XPS spectra of N 1s, the molar content of N in TiO_xN_y is about 6.8 mol%. XPS signals of O 1s (**Figure 24d**) are observed at around 530.4 eV and 532.0 eV, which can be assigned to Ti-O bond in TiO_2 and TiO_xN_y respectively [110, 111], indicating that the samples are composed of TiN and TiO_xN_y. The molar ratio of TiO_xN_y/TiN is determined by XPS to be 15.64, corresponding to the mass content of TiN to be 95 mass%. Since the content of TiO_xN_y was too low to be detected by XRD, these are not the diffraction peaks of TiO_xN_y XRD patterns.

4.2.2. Microstructure analyses

SEM images of TiN/TiO_xN_y obtained at 900°C for 4 h in partial cracked NH_3 are shown in **Figure 25**. It can be seen that the microstructure of TiO_xN_y/TiN nanoparticles duplicate the

http://dx.doi.org/10.5772/63487

original structure of the precursors. The average diameter of TiO_xN_y/TiN composite with solid microstructure is about 1–2 μm (**Figure 25b**). As shown in **Figure 25d**, yolk-shell TiO_xN_y/TiN are composed of a thin shell with an average thickness around 20 nm and a small yolk with an average diameter around 500 nm. As shown in **Figure 25f**, a thin shell with an average diameter around 1–2 μm and an average thickness around 20 nm combine the hollow microspheres.

TEM images of TiO_xN_y/TiN composite are shown in **Figure 26**. The low-magnification TEM images (**Figure 26a** and **b**) show that TiO_xN_y/TiN composite is composed of regular aggregated particles. As shown in **Figure 26c**, two particles firmly stick together, in which one lattice spacing is 0.40 nm and the other is 0.25 nm. The lattice spacing of two particles is consistent with the (111) planes of TiO_xN_y and the (111) planes of cubic TiN.

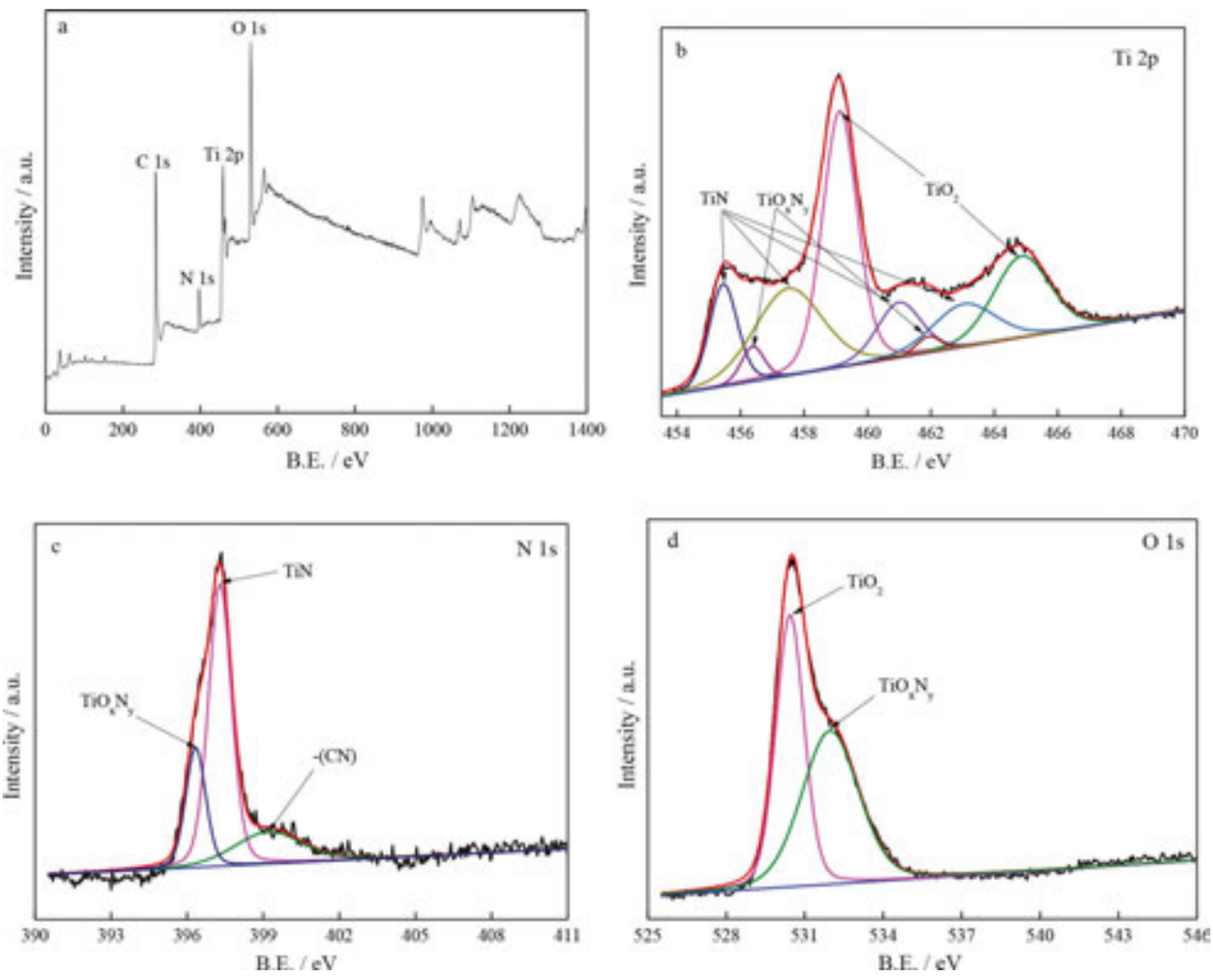

Figure 24. The full spectrum of XPS of the samples obtained at 900°C with 4 h (a), XPS spectra of (b) Ti 2p, (c) N 1s, (d) O 1s.

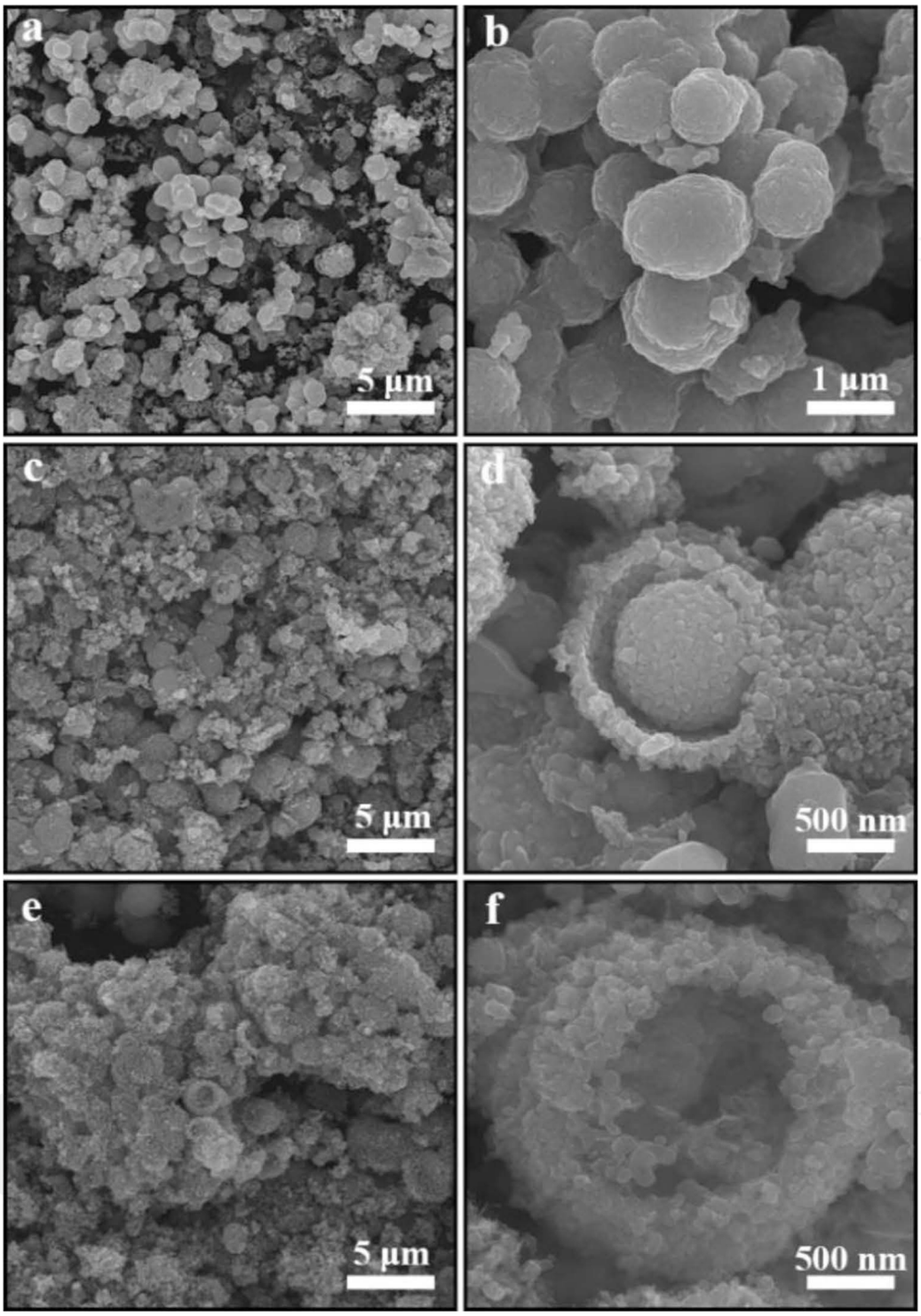

Figure 25. SEM photographs of TiO_xN_y/TiN composites: (a), (b) solid, (c), (d) yolk-shell, (e), (f) hollow.

In addition, it can be seen that TiN crystal is in close contact with TiO_xN_y crystal to form a heterojunction, which is believed to promote the transfer of photogenerated electrons and holes between TiN and TiO_xN_y, suppresses their recombination, and thus enhances the photocatalytic activity [115–117].

http://dx.doi.org/10.5772/63487

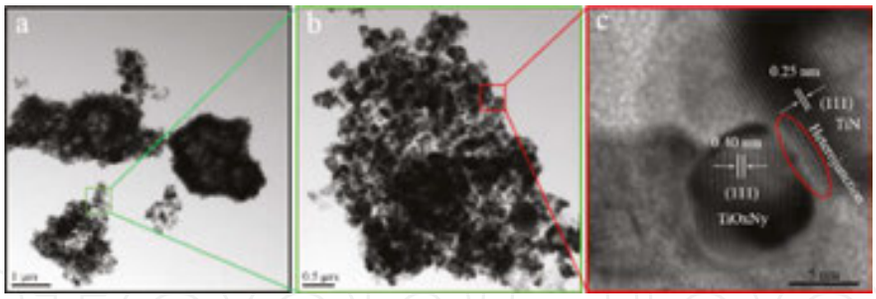

Figure 26. TEM photographs of TiO_xN_y/TiN composite.

4.2.3. Photocatalytic activities

The water splitting of H_2O to H_2 performance of solid TiO_xN_y/TiN, yolk-shell TiO_xN_y/TiN and hollow TiO_xN_y/TiN samples under light irradiation was examined in the presence of Na_2S and Na_2SO_3 as an hole acceptor. For comparison, the photocatalytic H_2 production of TiN and TiOxNy(N/Ti=2) is also carried out respectively. TiN was synthesized at 1000°C for 3 h in flowing partial cracked NH_3. TiOxNy (N/Ti=2) were synthesized through a microemulsion-hydrothermal method using triethylamine, urea, thiourea, and hydrazine as organic compounds [118]. The mixture is put in Teflon-lined stainless steel autoclave and heated at 120°C for 12 h. The results are shown in **Figure 27**. By comparison, the as-prepared TiO_xN_y/TiN heterojunction with yolk-shell and hollow structures exhibit better photocatalytic H_2 production activities, while the maximum H_2 production rate is achieved for yolk-shell TiO_xN_y/TiN with 35 μmol•h^{-1}•g^{-1}. The yolk-shell TiN synthesized at 800°C for 20 h was reported by Li's *et al.* group, which showed the larger visible-light-driven photocatalytic hydrogen production to be 22.8 μmol•h^{-1}•g^{-1}[98]. Our result is 1.5 times of that value. The recycling reaction experiments were carried out to investigate the stability of photocatalytic hydrogen production of yolk-shell TiO_xN_y/TiN under visible light irradiation. No decrease in catalytic activity is observed in the recycling reactions as shown in **Figure 27b**.

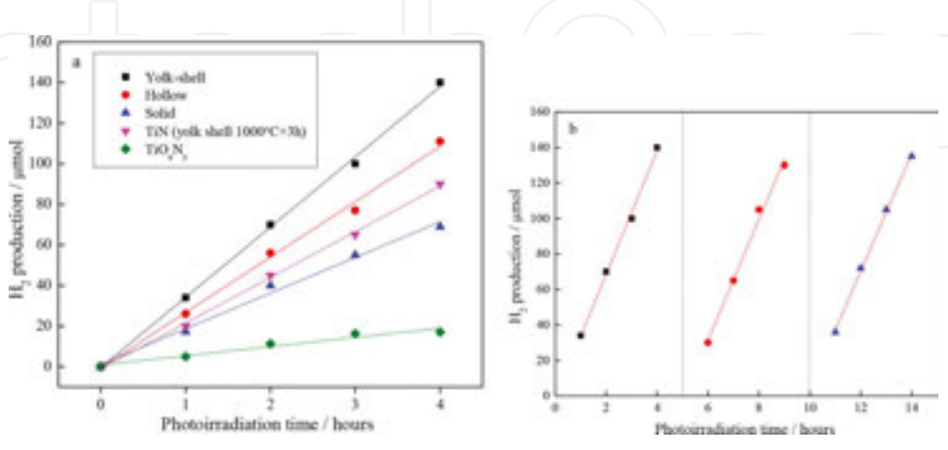

Figure 27. (a). Comparison of H_2 production rates of TiN, TiO_xN_y and TiO_xN_y/TiN heterojunction with different nanostructure. (b). Recycling test of the yolk-shell TiO_xN_y/TiN in the photocatalytic H_2 evolution.

The enhanced photocatalytic hydrogen production performance of the yolk-shell TiO_xN_y/TiN heterojunction is attributed to the formation of heterojunction by TiN and TiO_xN_y with the proper electronic structures and its special nanostructures. From the theoretical calculation as shown in **Figure 12**, TiN combining with TiO_xN_y with proper N doping concentration is expected to form favorable band-edge position, which may be a potential candidate for visible-light responsive photocatalyst. From XPS spectra, the molar content of N in TiO_xN_y is about 6.8 mol%, corresponding to the band gap of 1.56 eV. When TiN and TiO_xN_y is combined together, the band gap should be in the range of 0.8 and 1.56 eV. UV-Vis diffuse reflection spectra (**Figure 28**) is also carried out. The absorption band-edge for yolk-shell TiO_xN_y/TiN are at about 850 nm, corresponding to band gap energy to be 1.4 eV, verifying the theoretical calculation.

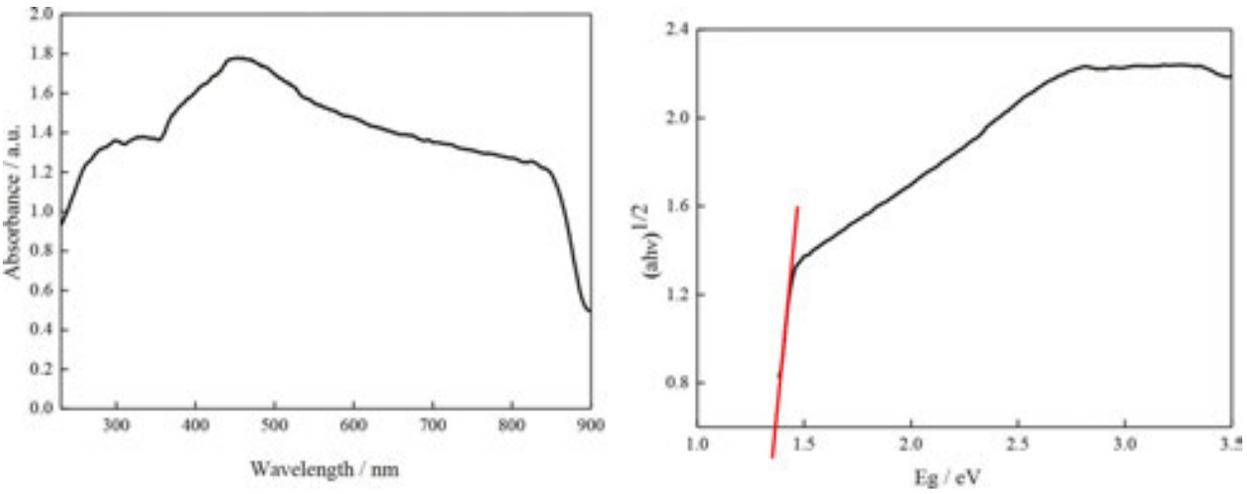

Figure 28. (a) UV-Vis diffuse reflection spectra of yolk-shell TiO_xN_y/TiN. (b) The plots of $(\alpha h\nu)^{1/2}$ versus hν. The band gap of yolk–shell TiO_xN_y/TiN.

Under visible-light irradiation, the photogenerated electrons are excited from the valence bands (VBs) to the conduction bands (CBs) of TiN and TiO_xN_y in the TiO_xN_y/TiN composite, creating positive holes in VB of TiN and TiO_xN_y (**Figure 29a**). Since CB (−0.6 eV)[12] level of TiN is lower than that of TiO_xN_y (CB: −0.4 eV) [119], electrons in CB of TiN can be transferred to that of TiO_xN_y. The VB (0.2 eV) [98] level of TiN is lower than that of TiO_xN_y (VB 0.6–1.1 eV) [119], holes in VB of TiO_xN_y can be transferred to that of TiN. Therefore, the probability of electron–hole recombination can be reduced, which can be confirmed by the photoluminescence spectra (**Figure 29b**). It is found that TiO_xN_y/TiN exhibits a fluorescence decrease (or quenching) as compared with TiN and TiO_xN_y [118], indicating that the photogenerated carrier recombination is inhibited greatly. These results should be derived from the imitate contacts between TiN and TiO_xN_y. Finally, the sacrificial reagents oxidized by the positive holes in the surface of TiN and the photo-excited electrons in the surface of TiO_xN_y can generate hydrogen, and thus the photocatalytic reaction can be enhanced greatly [60].

http://dx.doi.org/10.5772/63487

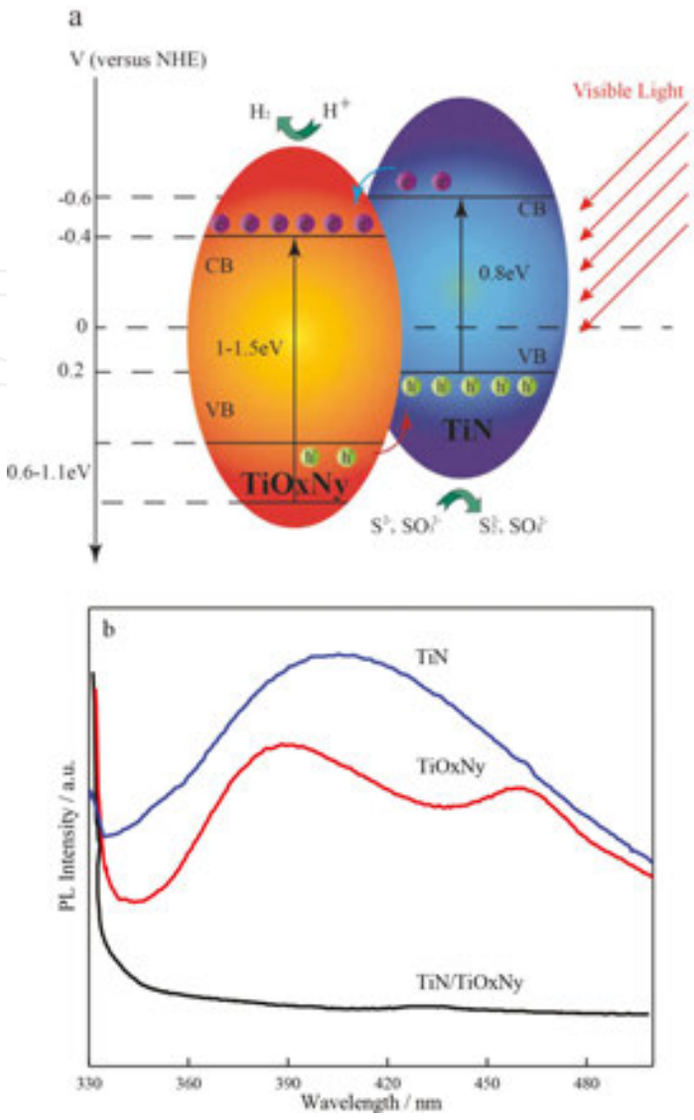

Figure 29. (a) Schematic diagram of photocatalytic mechanism for TiO_xN_y/TiN. (b) Photoluminescence spectra of TiO_xN_y/TiN.

Another important factor for the enhancement of the photocatalytic activities is the special yolk-shell nanostructures. First, the specific surface area of yolk-shell nanostructure is increased significantly, which increase the aqueous suspension contact area. Second, since the resulting yolk-shell nanostructures, there are the multiple light reflections within the chamber, which leads to efficient photocatalytic and photoelectro-chemical performances.

Therefore from above results, TiO_xN_y/TiN heterojunction composite with solid, yolk-shell, and hollow microspheres were prepared through reduction and nitridation of organotitania obtained through solvothermal alcoholysis. Especially, the yolk-shell TiO_xN_y/TiN heterojunction demonstrated an outstanding activity toward H_2 production as high as 34.9 $\mu mol \bullet h^{-1} \bullet g^{-1}$, which was about 1.5 times of the value reported in the literature. The electronic structure of heterojunction and the yolk-shell morphology are beneficial to enhance the H_2 production activity.

5. Summary and prospects

In our work including B-doped 3C-SiC nanowires and TiOxNy/TiN heterojunction composite, the electronic band structure, the crystallinity and crystal structure, surface structure, and morphology of photocatalysts on a nanometric scale had been investigated systematically and modified to optimize the preparation methods and refine the materials for maximizing efficiency. B-doped 3C-SiC NWs demonstrates an enhanced and stable activity for H_2 production as high as 108.4 μmol•h^{-1}, which is about 20 times of that of 3C-SiC, and 2.6 times of the value reported in the literature [99]. And the yolk-shell TiOxNy/TiN heterojunction demonstrated an outstanding activity toward H_2 production as high as 34.9 μmol•h^{-1}•g^{-1}, which was about 1.5 times of the value reported in the literature [98]. However, these improvements are not enough for industrial applications. Since the low photocatalytic efficiency and the lack of extensive studies for a successful scale-up of the laboratory setup into an industrially relevant scale. Therefore in the viewpoint of material and reactor design, reduction of cost will have to be given special priority before the final utilization of semiconductor-based photocatalytic hydrogen generation [120].

Acknowledgements

This study was supported by the National Science Fund for Excellent Young Scholars of China (No. 51522402), the National Natural Science Foundation of China (Grant No. 51572019)and the Central Universities of No. FRF-TP-13-006A and FRF-TP-15-006C1.

Author details

Tao Yang[1], Xinmei Hou[1*], Junhong Chen[2] and Kuo-Chih Chou[1]

*Address all correspondence to: houxinmei@ustb.edu.cn

1 State Key Laboratory of Advanced Metallurgy, University of Science and Technology Beijing, Beijing, China

2 School of Material Science and Engineering, University of Science and Technology Beijing, Beijing, China

References

[1] Crabtree, G.W. and N.S. Lewis, Solar energy conversion. Physics today, 2007. 60(3): pp. 37-42.

http://dx.doi.org/10.5772/63487

[2] Solangi, K.H., et al., A review on global solar energy policy. Renewable and Sustainable Energy Reviews, 2011. 15(4): pp. 2149-2163.

[3] Balat, M., Potential importance of hydrogen as a future solution to environmental and transportation problems. International Journal of Hydrogen Energy, 2008. 33(15): pp. 4013-4029.

[4] Wang, M., et al., The intensification technologies to water electrolysis for hydrogen production–A review. Renewable and Sustainable Energy Reviews, 2014. 29: pp. 573-588.

[5] Lu, Y.J., et al., Hydrogen production by biomass gasification in supercritical water: a parametric study. International Journal of Hydrogen Energy, 2006. 31(7): pp. 822-831.

[6] Navarro, R.M., M.A. Penaand and J. Fierro, Hydrogen production reactions from carbon feedstocks: fossil fuels and biomass. Chemical Reviews, 2007. 107(10): pp. 3952-3991.

[7] Cormos, C., et al., Innovative concepts for hydrogen production processes based on coal gasification with CO_2 capture. International Journal of Hydrogen Energy, 2008. 33(4): pp. 1286-1294.

[8] Cobden, P.D., et al., Sorption-enhanced hydrogen production for pre-combustion CO_2 capture: thermodynamic analysis and experimental results. International Journal of Greenhouse Gas Control, 2007. 1(2): pp. 170-179.

[9] Zhou, H., et al., The development of a new type of rechargeable batteries based on hybrid electrolytes. ChemSusChem, 2010. 3(9): pp. 1009-1019.

[10] Turner, J.A., A realizable renewable energy future. Science, 1999. 285(5428): pp. 687-689.

[11] Chen, X., et al., Semiconductor-based photocatalytic hydrogen generation. Chemical Reviews, 2010. 110(11): pp. 6503-6570.

[12] Esswein, A.J. and D.G. Nocera, Hydrogen production by molecular photocatalysis. Chemical Reviews, 2007. 107(10): pp. 4022-4047.

[13] Balzani, V., A. Credi and M. Venturi, Photochemical conversion of solar energy. ChemSusChem, 2008. 1(1-2): pp. 26-58.

[14] Fujishima, A. and K. Honda, Photolysis-decomposition of water at the surface of an irradiated semiconductor. Nature, 1972. 238(5385): pp. 37-38.

[15] Linsebigler, A.L., G. Lu and J.T. Yates Jr, Photocatalysis on TiO_2 surfaces: principles, mechanisms, and selected results. Chemical Reviews, 1995. 95(3): pp. 735-758.

[16] Reber, J.F. and M. Rusek, Photochemical hydrogen production with platinized suspensions of cadmium sulfide and cadmium zinc sulfide modified by silver sulfide. The Journal of Physical Chemistry, 1986. 90(5): pp. 824-834.

[17] Miseki, Y., et al., Cs-modified WO_3 photocatalyst showing efficient solar energy conversion for O_2 production and Fe (III) ion reduction under visible light. The Journal of Physical Chemistry Letters, 2010. 1(8): pp. 1196-1200.

[18] Erbs, W., et al., Visible-light-induced oxygen generation from aqueous dispersions of tungsten (VI) oxide. The Journal of Physical Chemistry, 1984. 88(18): pp. 4001-4006.

[19] Meissner, D., R. Memming and B. Kastening, Photoelectrochemistry of cadmium sulfide. 1. Reanalysis of photocorrosion and flat-band potential. The Journal of Physical Chemistry, 1988. 92(12): pp. 3476-3483.

[20] Erbs, W., et al., Visible-light-induced oxygen generation from aqueous dispersions of tungsten (VI) oxide. The Journal of Physical Chemistry, 1984. 88(18): pp. 4001-4006.

[21] Kalyanasundaram, K., et al., Cleavage of water by visible-light irradiation of colloidal CdS solutions; inhibition of photocorrosion by RuO_2. Angewandte Chemie International Edition in English, 1981. 20(11): pp. 987-988.

[22] Zhang, H. and Y. Zhu, Significant visible photoactivity and antiphotocorrosion performance of CdS photocatalysts after monolayer polyaniline hybridization. The Journal of Physical Chemistry C, 2010. 114(13): pp. 5822-5826.

[23] Yan, X., et al., Antiphotocorrosive photocatalysts containing CdS nanoparticles and exfoliated TiO_2 nanosheets. Journal of Materials Research, 2010. 25(01): pp. 182-188.

[24] Torimoto, T., et al., Photochemical shape control of cadmium sulfide nanorods coated with an amorphous silica thin layer. Journal of Nanoscience and Nanotechnology, 2009. 9(1): pp. 506-513.

[25] Solarska, R., et al., Tailoring the morphology of WO_3 films with substitutional cation doping: effect on the photoelectrochemical properties. Electrochimica Acta, 2010. 55(26): pp. 7780-7787.

[26] Gaillard, N., et al., Improved current collection in WO_3: Mo/WO_3 bilayer photoelectrodes. Journal of Materials Research, 2010. 25(01): pp. 45-51.

[27] Bär, M., et al., Mo incorporation in WO^3 thin film photoanodes: Tailoring the electronic structure for photoelectrochemical hydrogen production. Applied Physics Letters, 2010. 96(3): pp. 032107.

[28] Zaleska, A., et al., Photocatalytic activity of boron-modified TiO_2 under visible light: the effect of boron content, calcination temperature and TiO_2 matrix. Applied Catalysis B: Environmental, 2009. 89(3): pp. 469-475.

[29] Le Paven-Thivet, C., et al., Photoelectrochemical properties of crystalline perovskite lanthanum titanium oxynitride films under visible light. The Journal of Physical Chemistry C, 2009. 113(15): pp. 6156-6162.

http://dx.doi.org/10.5772/63487

[30] Yan, J., et al., Nitrogen-doped $SrTiO_3/TiO_2$ composite photocatalysts for hydrogen production under visible light irradiation. Journal of Alloys and Compounds, 2009. 472(1): pp. 429-433.

[31] Ravindranathan Thampi, K., Highly active meso–microporous TaON photocatalyst driven by visible light. Chemical Communications, 2005(2): pp. 268-270.

[32] Yashima, M., Y. Lee and K. Domen, Crystal structure and electron density of tantalum oxynitride, a visible light responsive photocatalyst. Chemistry of Materials, 2007. 19(3): pp. 588-593.

[33] Liu, M., et al., Water reduction and oxidation on Pt–Ru/$Y_2Ta_2O_5N_2$ catalyst under visible light irradiation. Chemical Communications, 2004(19): pp. 2192-2193.

[34] Higashi, M., et al., Two step water splitting into H_2 and O_2 under visible light by $ATaO_2N$ (A= Ca, Sr, Ba) and WO_3 with shuttle redox mediator. Chemical Physics Letters, 2008. 452(1): pp. 120-123.

[35] Qiu, X., Y. Zhao and C. Burda, Synthesis and characterization of nitrogen-doped group IVB visible-light-photoactive metal oxide nanoparticles. Advanced Materials-Deerfield Beach Then Weinheim-, 2007. 19(22): p. 3995.

[36] Kanade, K.G., et al., Rose-red color oxynitride $Nb_2Zr_6O_{17-x}N_x$: a visible light photocatalyst to hydrogen production. International Journal of Hydrogen Energy, 2007. 32(18): pp. 4678-4684.

[37] Matsumoto, Y., et al., N doping of oxide nanosheets. Journal of the American Chemical Society, 2009. 131(19): pp. 6644-6645.

[38] Shi, H., et al., 2-Propanol photodegradation over nitrogen-doped $NaNbO_3$ powders under visible-light irradiation. Journal of Physics and Chemistry of Solids, 2009. 70(6): pp. 931-935.

[39] Yang, T., et al., B-doped 3C-SiC nanowires with a finned microstructure for efficient visible light-driven photocatalytic hydrogen production. Nanoscale, 2015. 7(19): pp. 8955-8961.

[40] Li, W., et al., High-efficient degradation of dyes by $Zn_xCd_{1-x}S$ solid solutions under visible light irradiation. The Journal of Physical Chemistry C, 2008. 112(38): pp. 14943-14947.

[41] Wang, W., W. Zhu and H. Xu, Monodisperse, mesoporous $Zn_xCd_{1-x}S$ nanoparticles as stable visible-light-driven photocatalysts. The Journal of Physical Chemistry C, 2008. 112(43): pp. 16754-16758.

[42] Li, M., J. Jiang and L. Guo, Synthesis, characterization, and photoelectrochemical study of $Cd_{1-x}Zn_xS$ solid solution thin films deposited by spray pyrolysis for water splitting. International Journal of Hydrogen Energy, 2010. 35(13): pp. 7036-7042.

[43] Li, G., et al., Composition dependence of the photophysical and photocatalytic properties of ($AgNbO_3$) 1- x ($NaNbO_3$) x solid solutions. Journal of Solid State Chemistry, 2007. 180(10): pp. 2845-2850.

[44] Muktha, B., G. Madras and T.G. Row, A novel scheelite-like structure of $BaBi_2Mo_4O_{16}$: Photocatalysis and investigation of the solid solution, $BaBi_2Mo_{4-x}W_xO_{16}$($0.25 \leq x \leq 1$). Journal of Photochemistry and Photobiology A: Chemistry, 2007. 187(2): pp. 177-185.

[45] Maeda, K., et al., GaN: ZnO solid solution as a photocatalyst for visible-light-driven overall water splitting. Journal of the American Chemical Society, 2005. 127(23): pp. 8286-8287.

[46] Maeda, K., et al., Photocatalyst releasing hydrogen from water. Nature, 2006. 440(7082): pp. 295-295.

[47] Maeda, K., et al., Photocatalytic activity of ($Ga_{1-x}Zn_x$)($N_{1-x}O_x$) for visible-light-driven H_2 and O_2 evolution in the presence of sacrificial reagents. The Journal of Physical Chemistry C, 2008. 112(9): pp. 3447-3452.

[48] Maeda, K. and K. Domen, Solid solution of GaN and ZnO as a stable photocatalyst for overall water splitting under visible light†. Chemistry of Materials, 2009. 22(3): pp. 612-623.

[49] Yang, T., et al., Preparation of TiO_xN_y/TiN composites for photocatalytic hydrogen evolution under visible light. Physical Chemistry Chemical Physics, 2015. 17(43): pp. 28782-28788.

[50] Jing, D., Y. Zhang and L. Guo, Study on the synthesis of Ni doped mesoporous TiO_2 and its photocatalytic activity for hydrogen evolution in aqueous methanol solution. Chemical Physics Letters, 2005. 415(1): pp. 74-78.

[51] Ebina, Y., et al., Restacked perovskite nanosheets and their Pt-loaded materials as photocatalysts. Chemistry of Materials, 2002. 14(10): pp. 4390-4395.

[52] Ikuma, Y. and H. Bessho, Effect of Pt concentration on the production of hydrogen by a TiO_2 photocatalyst. International Journal of Hydrogen Energy, 2007. 32(14): pp. 2689-2692.

[53] Ogisu, K., et al., Lanthanum-indium oxysulfide as a visible light driven photocatalyst for water splitting. Chemistry Letters, 2007. 36(7): pp. 854-855.

[54] Ogisu, K., et al., Electronic band structures and photochemical properties of La- Ga-based oxysulfides. The Journal of Physical Chemistry C, 2008. 112(31): pp. 11978-11984.

[55] Jang, J.S., U.A. Joshi and J.S. Lee, Solvothermal synthesis of CdS nanowires for photocatalytic hydrogen and electricity production. The Journal of Physical Chemistry C, 2007. 111(35): pp. 13280-13287.

[56] Bao, N., et al., Highly ordered Pt-loaded CdS nanowire arrays for photocatalytic hydrogen production under visible light. Chemistry Letters, 2006. 35(3): pp. 318-319.

[57] Yuan, J., et al., Preparations and photocatalytic hydrogen evolution of N-doped TiO_2 from urea and titanium tetrachloride. International Journal of Hydrogen Energy, 2006. 31(10): pp. 1326-1331.

[58] Hitoki, G., et al., An oxynitride, TaON, as an efficient water oxidation photocatalyst under visible light irradiation ($\lambda \leq$ 500 nm). Chemical Communications, 2002(16): pp. 1698-1699.

[59] Xiao, W., et al., TiN film with (111) preferred orientation as a visible-light-driven photocatalyst for hydrogen evolution from water decomposition. Materials Chemistry and Physics, 2007. 105(1): pp. 6-9.

[60] Wang, H., et al., Semiconductor heterojunction photocatalysts: design, construction, and photocatalytic performances. Chemical Society Reviews, 2014. 43(15): pp. 5234-44.

[61] Spanhel, L., H. Weller and A. Henglein, Photochemistry of semiconductor colloids. 22. Electron ejection from illuminated cadmium sulfide into attached titanium and zinc oxide particles. Journal of the American Chemical Society, 1987. 109(22): pp. 6632-6635.

[62] Bickley, R.I., et al., A structural investigation of titanium dioxide photocatalysts. Journal of Solid State Chemistry, 1991. 92(1): pp. 178-190.

[63] Chen, X. and S.S. Mao, Titanium dioxide nanomaterials: synthesis, properties, modifications, and applications. Chemical Reviews, 2007. 107(7): pp. 2891-2959.

[64] Hidalgo, M.C., et al., Hydrothermal preparation of highly photoactive TiO_2 nanoparticles. Catalysis Today, 2007. 129(1): pp. 50-58.

[65] Testino, A., et al., Optimizing the photocatalytic properties of hydrothermal TiO_2 by the control of phase composition and particle morphology: a systematic approach. Journal of the American Chemical Society, 2007. 129(12): pp. 3564-3575.

[66] Datta, A., et al., Temperature tunability of size in CdS nanoparticles and size dependent photocatalytic degradation of nitroaromatics. Journal of Colloid and Interface Science, 2008. 322(1): pp. 128-135.

[67] GuiáYang, H., Nanosized anatase TiO_2 single crystals for enhanced photocatalytic activity. Chemical Communications, 2010. 46(5): pp. 755-757.

[68] Sun, W., et al., Studies on the enhanced photocatalytic hydrogen evolution over Pt/PEG-modified TiO_2 photocatalysts. International Journal of Hydrogen Energy, 2008. 33(4): pp. 1112-1117.

[69] Lee, Y., et al., Hydrothermal synthesis of fine $NaTaO_3$ powder as a highly efficient photocatalyst for overall water splitting. Bulletin of the Chemical Society of Japan, 2007. 80(2): pp. 423-428.

[70] Sathish, M., B. Viswanathan and R.P. Viswanath, Alternate synthetic strategy for the preparation of CdS nanoparticles and its exploitation for water splitting. International Journal of Hydrogen Energy, 2006. 31(7): pp. 891-898.

[71] Zhang, Z., et al., Role of particle size in nanocrystalline TiO_2-based photocatalysts. The Journal of Physical Chemistry B, 1998. 102(52): pp. 10871-10878.

[72] Serpone, N., et al., Subnanosecond relaxation dynamics in TiO_2 colloidal Sols (particle sizes Rp= 1.0-13.4 nm). relevance to heterogeneous photocatalysis. The Journal of Physical Chemistry, 1995. 99(45): pp. 16655-16661.

[73] Sun, T., J. Qiu and C. Liang, Controllable fabrication and photocatalytic activity of ZnO nanobelt arrays. The Journal of Physical Chemistry C, 2008. 112(3): pp. 715-721.

[74] Wang, W.W., Y.J. Zhu and L.X. Yang, ZnO–SnO_2 hollow spheres and hierarchical nanosheets: hydrothermal preparation, formation mechanism, and photocatalytic properties. Advanced Functional Materials, 2007. 17(1): pp. 59-64.

[75] Xu, T., et al., Monomolecular-layer $Ba_5Ta_4O_{15}$ nanosheets: synthesis and investigation of photocatalytic properties. Advanced Functional Materials, 2006. 16(12): p. 1599.

[76] Matsumoto, Y., S. Ida and T. Inoue, Photodeposition of metal and metal oxide at the TiO_x nanosheet to observe the photocatalytic active site. The Journal of Physical Chemistry C, 2008. 112(31): pp. 11614-11616.

[77] Ye, C., et al., Thickness-dependent photocatalytic performance of ZnO nanoplatelets. The Journal of Physical Chemistry B, 2006. 110(31): pp. 15146-15151.

[78] Zhang, C. and Y. Zhu, Synthesis of square Bi_2WO_6 nanoplates as high-activity visible-light-driven photocatalysts. Chemistry of Materials, 2005. 17(13): pp. 3537-3545.

[79] Harada, M., et al., Preparation and characterizations of Fe-or Ni-substituted titania nanosheets as photocatalysts. Journal of Photochemistry and Photobiology A: Chemistry, 2002. 148(1): pp. 273-276.

[80] Zhang, L., D. Chen and X. Jiao, Monoclinic structured $BiVO_4$ nanosheets: hydrothermal preparation, formation mechanism, and coloristic and photocatalytic properties. The Journal of Physical Chemistry B, 2006. 110(6): pp. 2668-2673.

[81] Sarahan, M.C., et al., $K_4Nb_6O_{17}$-derived photocatalysts for hydrogen evolution from water: nanoscrolls versus nanosheets. Journal of Solid State Chemistry, 2008. 181(7): pp. 1678-1683.

[82] Song, X. and L. Gao, Facile synthesis and hierarchical assembly of hollow nickel oxide architectures bearing enhanced photocatalytic properties. The Journal of Physical Chemistry C, 2008. 112(39): pp. 15299-15305.

[83] Lu, F., W. Cai and Y. Zhang, ZnO hierarchical micro/nanoarchitectures: solvothermal synthesis and structurally enhanced photocatalytic performance. Advanced Functional Materials, 2008. 18(7): pp. 1047-1056.

[84] Kale, B.B., et al., $CdIn_2S_4$ nanotubes and "Marigold" nanostructures: a visible-light photocatalyst. Advanced Functional Materials, 2006. 16(10): pp. 1349-1354.

[85] Zhang, J., et al., Self-assembled 3-D architectures of BiOBr as a visible light-driven photocatalyst. Chemistry of Materials, 2008. 20(9): pp. 2937-2941.

[86] Song, X. and L. Gao, Facile synthesis and hierarchical assembly of hollow nickel oxide architectures bearing enhanced photocatalytic properties. The Journal of Physical Chemistry C, 2008. 112(39): pp. 15299-15305.

[87] Fischer, T.H. and J. Almlof, General methods for geometry and wave function optimization. The Journal of Physical Chemistry, 1992. 96(24): pp. 9768-9774.

[88] Langreth, D.C. and M.J. Mehl, Beyond the local-density approximation in calculations of ground-state electronic properties. Physical Review B, 1983. 28(4): p. 1809.

[89] Becke, A.D., Density-functional exchange-energy approximation with correct asymptotic behavior. Physical review A, 1988. 38(6): p. 3098.

[90] Wang, Y. and J.P. Perdew, Correlation hole of the spin-polarized electron gas, with exact small-wave-vector and high-density scaling. Physical Review B, 1991. 44(24): p. 13298.

[91] Kressse, G. and J. Furthmüller, Efficient iterative schemes for ab initio total-energy calculations using a plane–wave basis set. Physical Review B, 1996. 54(16): pp. 11169-11186.

[92] Ceperley, D.M. and B.J. Alder, Ground state of the electron gas by a stochastic method. Physical Review Letters, 1980. 45(7): p. 566.

[93] Perdew, J.P. and A. Zunger, Self-interaction correction to density-functional approximations for many-electron systems. Physical Review B, 1981. 23(10): p. 5048.

[94] Vanderbilt, D., Soft self-consistent pseudopotentials in a generalized eigenvalue formalism. Physical Review B, 1990. 41(11): p. 7892.

[95] Hamann, D.R., M. Schlüter and C. Chiang, Norm-conserving pseudopotentials. Physical Review Letters, 1979. 43(20): p. 1494.

[96] DONG, L., et al., Synthesis and characterization of boron-doped SiC for visible light driven hydrogen production. Acta Physico-Chimica Sinica, 2014. 30(1): pp. 135-140.

[97] Agathopoulos, S., Influence of synthesis process on the dielectric properties of B-doped SiC powders. Ceramics International, 2012. 38(4): pp. 3309-3315.

[98] Li, G., et al., Mesoporous TiN microspheres with hierarchical chambers and enhanced visible light-driven hydrogen evolution. ChemSusChem, 2013. 6(8): pp. 1461-1466.

[99] Yang, J., et al., Photocatalytic water splitting to hydrogen production of reduced graphene oxide/SiC under visible light. Applied Physics Letters, 2013. 102(8): p. 083101.

[100] Tateyama, H., N. Sutoh and N. Murakawa, Quantitative-analysisofstacking-faultsinthestructureofsicbyx-ray-powderprofile refinementmethod. Nippon Seramikkusu

Kyokai Gakujutsu Ronbunshi-Journal of the Ceramic Society of Japan, 1988. 96(10): pp. 1003-1011.

[101] Shimoda, K., et al., Influence of surface structure of SiC nano-sized powder analyzed by X-ray photoelectron spectroscopy on basic powder characteristics. Applied Surface Science, 2007. 253(24): pp. 9450-9456.

[102] Oswald, S. and H. Wirth, Core-level shifts at B- and Al-doped 6H-SiC studied by XPS. Surface and Interface Analysis, 1999. 27(3): pp. 136-141.

[103] Lu, W., et al., Bismuth telluride hexagonal nanoplatelets and their two-step epitaxial growth. Journal of the American Chemical Society, 2005. 127(28): pp. 10112-10116.

[104] Zhu, Y.C., Y. Bando and L.W. Yin, Design and fabrication of BN-sheathed ZnS nanoarchitectures. Advanced Materials, 2004. 16(4): pp. 331-334.

[105] Yin, L.W., et al., Growth and field emission of hierarchical single-crystalline wurtzite AlN nanoarchitectures. Advanced Materials, 2005. 17(1): pp. 110-114.

[106] Speiser, R., S. Naiditch and H.L. Johnston, The vapor pressure of inorganic substances. II. B2O31. Journal of the American Chemical Society, 1950. 72(6): pp. 2578-2580.

[107] Gao, Y., Y. Wang and Y. Wang, Photocatalytic hydrogen evolution from water on SiC under visible light irradiation. Reaction Kinetics and Catalysis Letters, 2007. 91(1): pp. 13-19.

[108] Hao, J., et al., Photocatalytic hydrogen production over modified SiC nanowires under visible light irradiation. International Journal of Hydrogen Energy, 2012. 37(20): pp. 15038-15044.

[109] Chen, J., et al., Band gap characterization and photoluminescence properties of SiC nanowires. Applied Physics A, 2011. 102(1): pp. 213-217.

[110] Drygas, M., et al., Two-stage aerosol synthesis of titanium nitride TiN and titanium oxynitride TiO_xN_y nanopowders of spherical particle morphology. Chemistry of Materials, 2006. 18(13): pp. 3122-3129.

[111] Zukalova, M., et al., Facile conversion of electrospun TiO_2 into titanium nitride/oxynitride fibers. Chemistry of Materials, 2010. 22(13): pp. 4045-4055.

[112] Prabakar, K., et al., Effect of nitrogen on the photocatalytic activity of TiO_xN_y thin films. Journal of Vacuum Science and Technology A, 2006. 24(4): pp. 1156-1160.

[113] Trenczek-Zajac, A., et al., Structural and electrical properties of magnetron sputtered Ti (ON) thin films: the case of TiN doped in situ with oxygen. Journal of Power Sources, 2009. 194(1): pp. 93-103.

[114] Di Valentin, C., et al., N-doped TiO_2: theory and experiment. Chemical Physics, 2007. 339(1): pp. 44-56.

http://dx.doi.org/10.5772/63487

[115] Mondal, C., et al., Preformed ZnS nanoflower prompted evolution of CuS/ZnS p–n heterojunctions for exceptional visible-light driven photocatalytic activity. New Journal of Chemistry, 2015. 39(7): pp. 5628-5635.

[116] Yu, J., J. Zhang and S. Liu, Ion-exchange synthesis and enhanced visible-light photoactivity of CuS/ZnS nanocomposite hollow spheres. The Journal of Physical Chemistry C, 2010. 114(32): pp. 13642-13649.

[117] Yu, J. and B. Wang, Effect of calcination temperature on morphology and photoelectrochemical properties of anodized titanium dioxide nanotube arrays. Applied Catalysis B: Environmental, 2010. 94(3): pp. 295-302.

[118] Cong, Y., et al., Synthesis and characterization of nitrogen-doped TiO_2 nanophotocatalyst with high visible light activity. The Journal of Physical Chemistry C, 2007. 111(19): pp. 6976-6982.

[119] Wang, W., O. Savadogo and Z. Ma, Preparation of new titanium oxy nitride based electro catalysts using an anhydrous sol-gel method for water electrolysis in acid medium. International Journal of Hydrogen Energy, 2012. 37(9): pp. 7405-7417.

[120] Jing, D., et al., Efficient solar hydrogen production by photocatalytic water splitting: from fundamental study to pilot demonstration. International Journal of Hydrogen Energy, 2010. 35(13): pp. 7087-7097.

IntechOpen